Ocean Tide Modeling in the Southern Ocean

by

Yu Wang

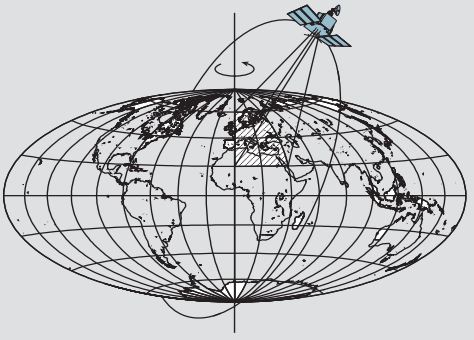

Report No. 471

Geodetic and GeoInformation Science
Department of Civil and Environmental Engineering and Geodetic Science
The Ohio State University
Columbus, Ohio 43210-1275

December 2004

OCEAN TIDE MODELING IN THE SOUTHERN OCEAN

by

Yu Wang

Report No. 471

Department of Civil and Environmental Engineering and Geodetic Science
The Ohio State University
Columbus, Ohio 43210

December 2004

ABSTRACT

Ocean tide has been observed and studied for a long time. With its role in the complex interactions between solid earth, ocean, sea ice and the floating glacial ice shelves, tides have been identified as one of the important causes of grounding line migration, an essential factor to the study of ice mass balance and global sea level change. In addition, accurate knowledge of ocean tides is needed for studies such as tidal mixing and sea ice calving. Polar ocean tide models remain poorly understood despite of the success of global ocean tide modeling in the deep oceans. In this thesis, a study of ocean tide modeling in the Southern Ocean employing the empirical tide solution approach is presented using the multiple satellite altimetry data at crossover locations.

The tidal aliasing problem in satellite altimetry is first investigated by testing the software for two frequency searching methods using simulated and actual altimetry data at crossover locations. Numerical experiments show that the software for the interval method performs better than that for the global optimization frequency searching method, by which the true original (not aliased) frequencies of the tides can be extracted from altimetry data at crossover locations. Also, using altimetry data at crossover locations can better reduce tidal aliasing than using along-track altimetry data.

Altimetry data at T/P and ERS-2 dual satellite crossovers for the Southern Ocean are generated using 300 cycles of T/P data and 79 cycles of ERS-2 data. Using these data, an empirical ocean tide solution is derived using the orthotide formulations. Different weighting methods are tested, and the use of different weights at different locations is adopted as our solution strategy. The empirical tide solutions have been evaluated by comparison with several other models, including the global tide models NAO99, TPXO.6.2 and the regional model CATS02.01. The comparison shows that our solution is comparable with the selected models. The *RSS* of 8 major short-period ocean tides between our solution using altimetry data at dual satellite crossover locations and the selected models is 2.2 ~ 2.4 cm. And when compared with selected models in terms of standard deviation of the sea surface height residuals, our solution shows improved performance with a tidal power of $2^2 \sim 4^2$ cm^2 improvement over the selected models.

PREFACE

This report was prepared by Yu Wang, a graduate research associate in the Department of Civil and Environmental Engineering and Geodetic Science at the Ohio State University, under the supervision of Professor C. K. Shum. This report was supported by a grant from the National Science Foundation Office of Polar Program: OPP-0088029.

This report was also submitted to the Graduate School of the Ohio State University as a thesis in partial fulfillment of the requirements for the Master of Science degree.

ACKNOWLEDGMENTS

I would like to express my sincere thanks to my adviser, Prof. C.K. Shum for his support, encouragement, and patient guidance, which led me into the field of ocean tide. Thanks go to Prof. Burkhard Schaffrin and Dr. Yuchan Yi for their time and valuable comments on my thesis work. I would like to thank Dr. Rainer Mautz, a visiting scholar at the Laboratory for Space Geodesy and Remote Sensing, Dr. Laurence Padman in ESR and Dr. Ole Andersen in KMS for their kind help in providing their software and models.

TABLE OF CONTENT

Page

LIST OF TABLES

LIST OF FIGURES

Figure **Page**

CHAPTER 1

INTRODUCTION

Every day, the sea rises and falls along the coasts around the world oceans. These phenomena had long been recognized as tides, the effects produced by the gravitational attraction of the Moon and the Sun on the Earth.

Historically, because of the importance for commerce, tides had been observed and predicted at the tide gauges along coastal regions with intense commercial activity. In 1687, Newton established the equilibrium theory, which explained the forces that generate the tides. Almost a century later, in 1775, Marquis P.S. Laplace published the dynamic response concept of ocean tides formulated in Laplace Tidal Equations (LTE). Since the solutions of these LTE strongly depend on the bathymetry and the shape of the ocean's boundaries, it is impossible to obtain analytical solutions. In the 19th century, the harmonic analysis method developed by Darwin (1883) provided an efficient way for tidal analysis and prediction.

The acquisition of long-term tide gauge observations, the invention of deep-ocean bottom pressure recorders in the mid 1960's, and the application of modern computers and numerical methods, improved our understanding of ocean tides. However, our knowledge of ocean tides remained to be limited in the vicinity of coastlines and mid-ocean islands where *in situ* measurements (i.e. from coastal tide gauges) are available. It was not until late 1970s that the advent of satellite altimetry offered, for the first time, a means to estimate ocean tides globally.

With the high precision and globally distributed satellite altimeter measurements, it is possible to extract ocean tide signals from satellite altimetry by suitable analysis of the altimeter data or by assimilation of altimeter data into the hydrodynamic models. Since one of the first evidences of the tide signal in altimeter data was shown from Seasat (Le Provost, 1983), new ocean tide models have been developed. Based on 2.5 years of altimetry data from Geosat Exact Repeat Mission, Cartwright and Ray (1990, 1991) obtained the first altimetry-derived global tide solution which is more accurate than Schwiderski's model (1980), which had been derived by solving the hydrodynamic LTE equations and had been widely used more than a decade before. The launch of an unprecedented precise satellite altimeter TOPEX/POSEIDON (T/P) promoted the generation of more global tide models; and with the accumulation of altimetry data from T/P and improvement in numerical methods, these models have been revised with better accuracy, such as the FES model series (e.g. FES94, FES95, FES98, FES99, FES2002), the CSR model series (e.g. CSR3.0, CSR4.0), the GOT models (e.g. GOT99, GOT00), the DW model, the NAO model and many others.

In general, the modern global tide models can be categorized into three groups:

empirical model, hydrodynamic model and assimilation model. Although all these T/P-derived tide models have an accuracy of 2-3 cm in deep oceans (Shum et al., 1997, 2001), they are still problematic in coastal and shallow water areas (Shum et al., 2001). Due to the latitude limit and other design characteristics of the satellite altimeter, the altimetry data from T/P have the coverage only within $\pm 66^{o}$ latitude. The altimeter cannot measure accurately close to shorelines and over oceans with non-permanent or seasonal ice covers. As a result, contemporary global tide models are confined to the region of $\pm 66^{o}$ latitude and, for the region beyond T/P coverage, these models are primarily constrained by prediction from hydrodynamic solutions (e.g. FES94 model). All of these factors resulted in our comparatively poor knowledge of tides in the polar region and underneath the ice shelves. However, non-T/P altimetry data which cover the region beyond $\pm 66^{o}$ limit, such as the datasets from the ERS-1/2, Geosat, GFO and Envisat missions, may contribute to the ocean tide modeling in the polar region. Also, the measurements from other techniques, such as GPS and InSAR, may provide possible ways to detect the tidal motion in polar regions and ice-covered oceans (Aoki et al., 2001; Rignot et al., 2000; Shum et al., 2001). But non-T/P altimetry data are less accurate because of their lower altitude and single-frequency altimeters, and that their orbits are not optimized for minimizing tidal aliasing. How to combine these data with T/P data to improve the spatial resolution, coverage and even the accuracy of ocean tide models, is still an open problem.

In this thesis, we carry out a study on the ocean tide modeling for the Southern Ocean, which is defined as reaching from -50^{o} latitude to south poleward, by investigating the possible combination of ERS-2 data with T/P data at the crossover locations using the orthotide method (Groves and Reynolds, 1975), which is the orthogonalized form of the response method with mutually orthogonal orthotide functions. The purpose is to improve spatial resolutions, reduce tidal aliasing using non-T/P data and develop techniques for dual-satellite crossovers associated with other high-latitude observing altimeters. A brief review of tide theory is provided in Chapter 2, including the tide generating potential, the harmonic expansion and two kinds of tidal analysis methods. In Chapter 3, introductions to satellite altimetry and ocean tide modeling are presented with descriptions of several ocean tide models. Chapter 4 provides results of our investigation into the problem of tidal aliasing. Then in Chapter 5, our study on the ocean tide modeling for the Southern Ocean is described, and the results of an empirical tide solution are presented and analyzed. Finally, conclusions and plans for future work are summarized in Chapter 6.

CHAPTER 2

OCEAN TIDE THEORY

Tides are caused by the gravitational forces of the Sun and the Moon on the non-rigid Earth. The tide-generating potential from which these forces may be derived will be concisely reviewed in Section 2.1. The development of the tide-generating potential in a series of harmonics will be introduced in Section 2.2. Two techniques in tidal analysis will be presented in Section 2.3.

2.1 Tide-generating potential

Due to the gravitational attraction of the Sun and the Moon, the surface of the elastic Earth will deform periodically, which phenomenon is known as tides. The mass redistribution of the Earth will result in the variation of the geopotential, in which the tide-generating potential *U* on the surface of the Earth caused by the attracting body, the Sun or the Moon, can be expressed as

$$U(R_e,\phi,\lambda)=\frac{GM}{R}\sum_{l=2}^{\infty}\left(\frac{R_e}{R}\right)^l P_l(\cos\theta) \tag{2.1}$$

where *GM* is the product of the universal gravitational constant and the mass of the attracting body, R_e is the mean radius of the Earth, R and θ are the geocentric distance and the zenith distance from the point (R_e,ϕ,λ) of the attracting body, respectively. $P_l(\cos\theta)$ is the Legendre polynomial of degree l. Since the ratio R_e/R denotes the sine of the parallax (π) of the attracting body (ref. Figure 2.1), which has very small values for the Moon and the Sun (Taff, 1985), only the term with $l=2$ in (2.1) is generally considered as representing the tide-generating potential, although sometimes the term with $l=3$ is also taken into account for the Moon. So we have the main term of the tide generating potential as

$$U_2(R_e,\phi,\lambda)=\frac{3GMR_e^2}{4R^3}(\cos 2\theta+\frac{1}{3}) \tag{2.2}$$

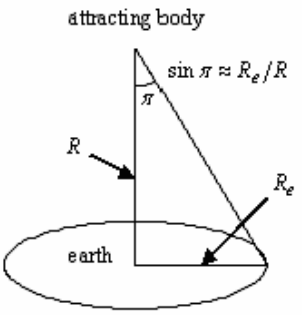

Figure 2.1 Illustration of parallax

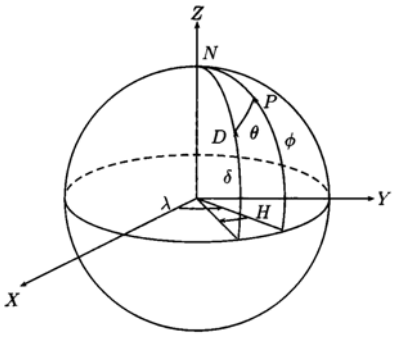

Figure 2.2 Spherical triangle NPD

Using the spherical triangle NPD (see Figure 2.2) which involves the zenith distance θ of the attracting body D, the geocentric longitude λ and latitude ϕ of a location P on the surface of the Earth, and the right ascension α and declination δ of the attracting body, one obtains

$$\cos\theta = \sin\phi\sin\delta + \cos\phi\cos\delta\cos H \tag{2.3}$$

where

$$H = \theta'_g + \lambda - \alpha \tag{2.4}$$

is the hour angle of the attracting body (α, δ) at the observer site (λ, ϕ), with θ'_g as the Greenwich sidereal time. Thus $P_l(\cos\theta)$ can be expressed as

$$P_l(\cos\theta) = \sum_{m=0}^{l}(2-\delta_{0m})\frac{(l-m)!}{(l+m)!}P_{lm}(\sin\phi)P_{lm}(\sin\delta)\cos(mH) \tag{2.5}$$

and the tide-generating potential can be written in the following form

$$U(R_e,\phi,\lambda) = \frac{GM}{R}\sum_{l=2}^{\infty}(\frac{R_e}{R})^l\sum_{m=0}^{l}(2-\delta_{0m})\frac{(l-m)!}{(l+m)!}P_{lm}(\sin\phi)P_{lm}(\sin\delta)\cos(mH) \tag{2.6}$$

where δ_{0m} is the Kronecker delta and $P_{lm}(\sin\phi)$, $P_{lm}(\sin\delta)$ are the associated Legendre functions. The corresponding main part of the tide-generating potential is written as

$$U_2(R_e,\phi,\lambda)=\sum_{m=0}^{2}U_{2m}(R_e,\phi,\lambda)$$
$$=\frac{3GMR_e^2}{4R^3}\left\{\cos^2\phi\cos^2\delta\cos 2H+\sin 2\phi\sin 2\delta\cos H+(1-3\sin^2\phi)(\frac{1}{3}-\sin^2\delta)\right\} \tag{2.7}$$

Obviously, from (2.7) we can see that the first term with $m=2$ is the semi-diurnal species, the second term with $m=1$ is the diurnal species and the third term with $m=0$ is the long-period species.

2.2 Expansion of the tide-generating potential

From (2.6), it follows that the tide-generating potential is also a function of the position of the attracting body, here, the Sun and the Moon. Since the motion of the Sun and the Moon can be described by several astronomical angles which approximately proceed linearly with time, the tide-generating potential can be developed into a series of harmonics.

Following the first development of harmonic expansion by G. H. Darwin (1883), A. T. Doodson (1921) provided the first complete development of the tide generating potential by using E.W. Brown's lunar theory and expansions for the longitude and latitude of the Moon referred to the ecliptic rather than to the orbit. Each species U_{2m} in the 2nd degree term U_2 of the tide generating potential can be written as

$$U_{2m}=G_m(\phi)\sum_k|\eta_k|\cos(\theta_k+\chi_k+m\lambda)=\mathrm{Re}\left[G_m(\phi)e^{im\lambda}\sum_k|\eta_k|e^{i(\theta_k+\chi_k)}\right] \tag{2.8}$$

where $\mathrm{Re}[\ ]$ denotes the real part of $[\ ]$. $G_m(\phi)$ are Doodson's geodetic coefficients, namely

$$G_0(\phi)=\frac{3GMR_e^2}{4\overline{R}^3}(\frac{1}{2}-\frac{3}{2}\sin^2\phi)$$
$$G_1(\phi)=\frac{3GMR_e^2}{4\overline{R}^3}\sin 2\phi \tag{2.9}$$
$$G_2(\phi)=\frac{3GMR_e^2}{4\overline{R}^3}\cos^2\phi$$

$\overline{R}$ is the mean distance from the Moon or the Sun to the Earth. η_k are the coefficients of the harmonic expansion. χ_k are additive phase corrections, which are multiples of

$\pi/2$ and introduced to modify the phase to make (2.8) a series of all-positive coefficients $|\eta_k|$ and cosine functions only (Casotto, 1989). The symbols θ_k denote the Doodson arguments at Greenwich, and are expressed as

$$\theta_k(t) = A\tau + Bs + Ch + Dp + EN' + Fp_s \tag{2.10}$$

where $N' = -N$, $\tau = t - s + h$ and t, s, h, p, N, p_s are the fundamental angles that represent Greenwich mean solar time, mean longitude of the Moon, the Sun, the lunar perigee, the lunar node, and the solar perigee, respectively. The variation of s, h, p, N and p_s can be expressed as polynomials of time (in units of Julian century) based on Brown's lunar theory and Newcomb's theory of the Sun (Doodson, 1921; Casotto, 1989; Smith, 1999). The combination

$$k_1 k_2 k_3 . k_4 k_5 k_6 = A(B+5)(C+5).(D+5)(E+5)(F+5) \tag{2.11}$$

is known as Doodson number, which is introduced to denote each tide constituent. The frequency of the tide constituent is given by

$$\dot{\theta}_k = A\dot{\tau} + B\dot{s} + C\dot{h} + D\dot{p} + E\dot{N}' + F\dot{p}_s \tag{2.12}$$

In the 1970's, using the new precise lunar and solar ephemerides and astronomical constants as well as the calculation by computers, Cartwright and Tayler (1971), Cartwright and Edden (1973), recalculated the potential with their expansion in the following form, which arose from the response method of Munk and Cartwright (1966):

$$U(R_e, \phi, \lambda) = \mathrm{Re}\left[g \sum_{l=2}^{\infty} \sum_{m=0}^{l} c_{lm}^{*}(t) W_{lm}(\lambda, \phi) \right] \tag{2.13}$$

where g is the Earth's mean gravity acceleration, and $W_{lm}(\lambda, \phi)$ are the spherical harmonics, defined as

$$W_{lm}(\lambda, \phi) = (-1)^m \sqrt{\frac{2l+1}{4\pi} \frac{(l-m)!}{(l+m)!}} P_{lm}(\sin\phi) e^{im\lambda} \tag{2.14}$$

The time-varying coefficient c_{lm}^{*} (* denotes the complex conjugate) corresponds to the Greenwich equilibrium tide of degree l and order m. For $l = 2$,

$$c_{2m}^{*} = (-1)^{m+\delta_{0m}} \sum_k |B_k| e^{i(\theta_k + \chi_k)} \tag{2.15}$$

where the symbols B_k denote the equilibrium amplitudes as tabulated in Cartwright and Tayler (1971), Cartwright and Edden (1973). The term $(-1)^{m+\delta_{0m}}$ is introduced to obtain all-positive amplitudes $|B_k|$ and cosine arguments in the harmonic expansions.

2.3 Tidal analysis

Under the tide force derived from the tide-generating potential, the water mass on the surface of the Earth will have a vertical movement. By definition, ocean tide is the vertical displacement of the sea level above the moving ocean floor. From equilibrium theory, the ocean tide will follow an equilibrium response under the tide generating potential U. The vertical displacement (called equilibrium tide) is given by U/g. But since the Earth is not a rigid body or entirely covered with water, it is not appropriate to assume that the ocean tide follows the equilibrium response although long-period tides, which have a period of a month or longer, may be expected to closely follow the equilibrium theory (Lambeck, 1988). So equilibrium theory has major limitations in ocean tide modeling, but it does serve as an important reference in tidal analysis (e.g. in response analysis).

In 1775, Marquis P. S. Laplace established the Laplace Tidal Equations (LTE) to describe the motion of the water mass as a result of tidal forces, which provide a dynamical theory to express the ocean tide.

2.3.1 Harmonic analysis

At time t, the harmonic expression of the ocean tidal height at location (λ,ϕ) can be written as

$$\zeta(\lambda,\phi,t) = \sum_k H_k(\lambda,\phi)\cos[\theta_k(t) + \chi_k - G_k(\lambda,\phi)] \tag{2.16}$$

where $H_k(\lambda,\phi)$, $G_k(\lambda,\phi)$ are the unknown amplitude and Greenwich phase lag of tide k at location (λ,ϕ). θ_k and χ_k are the same as in (2.8).

For the purpose of solving the unknown amplitude H_k and phase lag G_k through the least squares estimation procedure, and to avoid the singularities of the amplitude at the amphidromes, it is more common to give (2.16) the following form using cosine and sine function:

$$\zeta(\lambda,\phi,t) = \sum_k [C_k(\lambda,\phi)\cos(\theta_k(t)+\chi_k) + S_k(\lambda,\phi)\sin(\theta_k(t)+\chi_k)] \tag{2.17}$$

where

$$\begin{aligned} C_k &= H_k \cos(G_k) \\ S_k &= H_k \sin(G_k) \end{aligned} \tag{2.18}$$

are called cosine, sine terms or inphase, quadrature terms associated with tide constituent k. Thus their relation to the amplitude and phase lag can be obtained by

$$\begin{aligned} H_k &= \sqrt{C_k^2 + S_k^2} \\ G_k &= \arctan(\frac{S_k}{C_k}) \end{aligned} \tag{2.19}$$

To account for the nodal correction on the lunar tide, lunar nodal modulation factors are introduced to the harmonic expression of the tidal height (Munk and Cartwright, 1966; Schureman, 1971; Schwiderski, 1980):

$$\zeta(\lambda,\phi,t) = \sum_k f_k C_k(\lambda,\phi)\cos(\theta_k(t)+\chi_k+\mu_k) + f_k S_k \sin(\theta_k(t)+\chi_k+\mu_k) \tag{2.20}$$

Here f_k is the nodal factor, μ_k is the nodal angle. Both of them depend on the position of the lunar node and hence vary slowly with time in the 18.6-year nodal period. The nodal correction only applies to lunar tide. So, for solar tide, $f_k = 1$, $\mu_k = 0$.

2.3.2 Response analysis

Although harmonic analysis provides a convenient way to solve the tidal parameters (e.g. C_k, S_k), it has some limitations in data duration and resolvability of terms close in frequency. Munk and Cartwright (1966) introduced the so-called response method, which expresses the ocean tide as the convolution of the equilibrium tide and a weight function. Considering only the main tidal constituents ($l = 2$), the ocean tide height ζ at time t and at location (λ,ϕ) is given by

$$\zeta(\lambda,\phi,t) = \mathrm{Re}\left[\sum_{m=0}^{2} c_{2m}^*(t) * w_{2m}(\lambda,\phi,t)\right] \tag{2.21}$$

where

$$c_{2m}^*(t) = a_{2m}(t) - ib_{2m}(t) \tag{2.22}$$

is the second-order equilibrium tide as in (2.15), and

$$w_{2m}(\lambda,\phi,t)=\sum_{s=-S}^{S}w_{2ms}(\lambda,\phi)\delta(t-s\Delta T) \tag{2.23}$$

is the weight function. With the response weight w_{2ms} written as

$$w_{2ms}(\lambda,\phi)=u_{2ms}(\lambda,\phi)+iv_{2ms}(\lambda,\phi) \tag{2.24}$$

(2.21) can be given the form

$$\zeta(\lambda,\phi,t)=\sum_{m=0}^{2}\sum_{s=-S}^{S}[u_{2ms}(\lambda,\phi)a_{2m}(t-s\Delta T)+v_{2ms}(\lambda,\phi)b_{2m}(t-s\Delta T)] \tag{2.25}$$

In the above expressions, $\delta(t)$ is the Dirac's unit impulse. ΔT is the lag interval, usually taken as 2 days. S determines the number of response weights that will be considered, in general $S=1$ or 2. The negative value of *s* has no physical meaning, but is of mathematical advantage.

Since nodal modulation factors have been implicitly contained in c_{2m}^{*}, there are no nodal correction parameters in (2.25). Thus, the response weight (u_{2ms},v_{2ms}) in (2.25), which defines the admittance function, could be solved using a least squares procedure.

2.3.3 Admittance and orthotide

The admittance of a tide constituent with angular frequency $\dot{\theta}_k$ is defined as the Fourier transform of the weight function w_{2m}.

$$Z_{2m}(\dot{\theta}_k)=X_{2m}(\dot{\theta}_k)+iY_{2m}(\dot{\theta}_k)=\int_{-\infty}^{\infty}w_{2m}(t)e^{-i\dot{\theta}_k t}dt \tag{2.26}$$

Substituting (2.23), (2.24) into (2.26), one can get

$$Z_{2m}(\dot{\theta}_k)=\sum_{s=-S}^{S}(u_{2ms}+iv_{2ms})e^{-i\dot{\theta}_k s\Delta T} \tag{2.27}$$

and thus

$$X_{2m}(\dot{\theta}_k) = \sum_{s=-S}^{S}[u_{2ms}\cos(\dot{\theta}_k s\Delta T) + v_{2ms}\sin(\dot{\theta}_k s\Delta T)]$$
$$Y_{2m}(\dot{\theta}_k) = \sum_{s=-S}^{S}[v_{2ms}\cos(\dot{\theta}_k s\Delta T) - u_{2ms}\sin(\dot{\theta}_k s\Delta T)] \tag{2.28}$$

With the assumption of smoothness, the admittance function provides a way to derive a number of small tides by interpolating the smooth admittance which is well defined by the dominant tides. So, by evaluating only a few parameters, one obtains a complete definition of each species of tide, not limited by a selected set of harmonic constants. Such a small number of parameters also stabilize the tidal solution (Munk and Cartwright, 1966). Moreover, smooth admittance also makes it easy to separate tide constituents with close frequencies, which is difficult to do in harmonic analysis. With these advantages, the admittance parameters (2.28) provide an equivalent way to describe the tides compared with the harmonic coefficients (2.18). The following relation between admittance and harmonic coefficients has been given by (Cartwright and Ray, 1990; Smith, 1999):

$$C_k = (-1)^{m+\delta_{0m}}|B_k|X_{2m}(\dot{\theta}_k)$$
$$S_k = -(-1)^{m+\delta_{0m}}|B_k|Y_{2m}(\dot{\theta}_k) \tag{2.29}$$

where $|B_k|$ is the equilibrium amplitude as in (2.15).

Noticing that the terms a_{2m}, b_{2m} are generally not orthogonal, which may result in an ill-conditioned normal matrix for (2.25), Groves and Reynolds (1975) introduced the orthogonalized convolution method of tide prediction, in which the so-called orthotides replace the equilibrium tides used in (2.25). The tidal height is written as

$$\zeta(\lambda,\phi,t) = \sum_{m=0}^{2}\sum_{j=0}^{2S}[U_j^m(\lambda,\phi)P_j^m(t) + V_j^m(\lambda,\phi)Q_j^m(t)] \tag{2.30}$$

where $P_j^m(t)$, $Q_j^m(t)$ are the orthotide functions which are simple linear combinations of $a_{2m}(t-s\Delta T)$, $b_{2m}(t-s\Delta T)$ and all combinations of pairs from (P_i, P_j, Q_i, Q_j) are nearly orthogonal in time. $U_j^m(\lambda,\phi)$, $V_j^m(\lambda,\phi)$ are called orthoweights, which should be estimated by a least squares procedure.

In general, it is adequate to adopt $S=1$ to account for most of the tidal variance at several sites (Alcock and Cartwright, 1978; Cartwright and Ray, 1990). So for $l=2$, considering only the diurnal and semidiurnal terms, the orthotide formalism for the tidal height can be expressed as

$$\zeta(\lambda,\phi,t)=\sum_{m=1}^{2}\sum_{j=0}^{2}[U_j^m(\lambda,\phi)P_j^m(t)+V_j^m(\lambda,\phi)Q_j^m(t)] \tag{2.31}$$

where the first few orthotide functions are (Cartwright and Ray, 1990):

$$\begin{aligned}
P_0^m(t) &= p_{00}^m a_{2m}(t)\\
P_1^m(t) &= p_{10}^m a_{2m}(t) - p_{11}^m a_{2m}^+(t)\\
P_2^m(t) &= p_{20}^m a_{2m}(t) - p_{21}^m a_{2m}^+(t) + q_{21}^m b_{2m}^-(t)\\
Q_0^m(t) &= p_{00}^m b_{2m}(t)\\
Q_1^m(t) &= p_{10}^m b_{2m}(t) - p_{11}^m b_{2m}^+(t)\\
Q_2^m(t) &= p_{20}^m b_{2m}(t) - p_{21}^m b_{2m}^+(t) - q_{21}^m a_{2m}^-(t)
\end{aligned} \tag{2.32}$$

The coefficients p_{ij}^m, q_{ij}^m are specially computed and here listed in Table 2.1.

	Diurnal (m=1)	Semidiurnal (m=2)
p_{00}	0.0298	0.0200
p_{10}	0.1408	0.0905
p_{11}	-0.0805	-0.0638
p_{20}	0.6002	0.3476
p_{21}	-0.3025	-0.1645
q_{21}	0.1517	0.0923

Table 2.1 Orthotide coefficients

$a_{2m}^+(t)$, $a_{2m}^-(t)$, $b_{2m}^+(t)$, $b_{2m}^-(t)$ are defined as

$$\begin{aligned}
a_{2m}^{\pm}(t) &= a_{2m}(t+\Delta T) \pm a_{2m}(t-\Delta T)\\
b_{2m}^{\pm}(t) &= b_{2m}(t+\Delta T) \pm b_{2m}(t-\Delta T)
\end{aligned} \tag{2.33}$$

The transformation from the orthoweights U_j^m, V_j^m to the admittance terms is given by

Cartwright and Ray (1990) as:

$$X_{2m}(\dot{\theta}_k) = p_{00}^m U_0^m + [p_{10}^m - p_{11}^m c(\dot{\theta}_k)]U_1^m + [p_{20}^m - p_{21}^m c(\dot{\theta}_k) - q_{21}^m s(\dot{\theta}_k)]U_2^m$$
$$Y_{2m}(\dot{\theta}_k) = p_{00}^m V_0^m + [p_{10}^m - p_{11}^m c(\dot{\theta}_k)]V_1^m + [p_{20}^m - p_{21}^m c(\dot{\theta}_k) - q_{21}^m s(\dot{\theta}_k)]V_2^m \quad (2.34)$$

where

$$c(\dot{\theta}_k) = 2\cos(\dot{\theta}_k \Delta T)$$
$$s(\dot{\theta}_k) = 2\sin(\dot{\theta}_k \Delta T) \quad (2.35)$$

CHAPTER 3

SATELLITE ALTIMETRY AND OCEAN TIDE MODELING

3.1 Satellite altimetry

Before the availability of satellite altimetry, tide gauges have been the major data source for ocean tide modeling. But tide gauge measurements have some limitations due to the sparseness of the global tide gauge network and their locations along the coasts. Compared with tide gauges, satellite altimetry, which is characterized by nearly global coverage with an accuracy of a few centimeters, provides an efficient and new way to monitor sea level change and do tide modeling.

Satellite altimetry is a technique for measuring sea surface height. In general, when we talk about satellite altimetry, we mean satellite radar altimetry, which measures the travel time taken by a radar pulse to travel from the satellite antenna to the surface and back to the satellite receiver. Because of the favorable property of a relatively flat water surface, radar altimetry is designed to be especially suitable over the ocean. Nowadays, the satellite altimeter ICESat has been in operation since its launch in January 2003, which transmits laser pulses and is specifically designed to measure the changes in the thickness of the ice sheets in Antarctica and Greenland, and the elevations of both clouds and land. Measurement principles of satellite altimetry will be described in the following subsection.

3.1.1 Measurement principle of satellite altimetry

The concept of satellite altimetry was first proposed at the Williamstown Conference in 1969 (Kaula, 1969). Since the first satellite altimetry tests during the SKYLAB missions (1973-1974), new and improved altimetry missions have been developed and launched. In Table 3.1, a list of some of the past, present and future satellite altimetry missions is given with their orbital inclination and their repeat periods.

Mission	Launch time	Inclination (degree)	Repeat period (days)
GEOSAT	Mar., 1985	108	17
ERS-1	July, 1991	98.5	3, 35, 168 [a]
TOPEX/POSEIDON	Aug., 1992	66	9.9
ERS-2	Apr., 1995	98.5	35
GFO	Feb., 1998	108	17
JASON-1	Dec., 2001	66	9.9
ENVISAT	Mar., 2002	98.5	35
ICESat	Jan., 2003	94	8, 183 [b]
CRYOSAT	Mar., 2005	92	2, 369[c]

a. The three repeat periods correspond to the mission phases of calibration and ice-sea observation, ocean observation, and geodetic observation, respectively.

b. The verification orbit has the 8-days repeat period, and the mission orbit has the 183-days repeat period.

c. The repeat period is 369 days with 30 days sub-cycle. For validation-orbit phase, the repeat period is 2 days,

Table 3.1 Satellite altimetry missions

The measurement principle of satellite altimetry is relatively straightforward which involves the geometry illustrated in Figure 3.1 and expressed in (3.1):

$$h_{ssh} = h_{orb} - h_{alt} \tag{3.1}$$

where h_{ssh} is the sea surface height with respect to the reference ellipsoid, h_{orb} is the satellite altitude above the reference ellipsoid and h_{alt} is the range from the satellite altimeter to the instant sea surface, all at time of measurement.

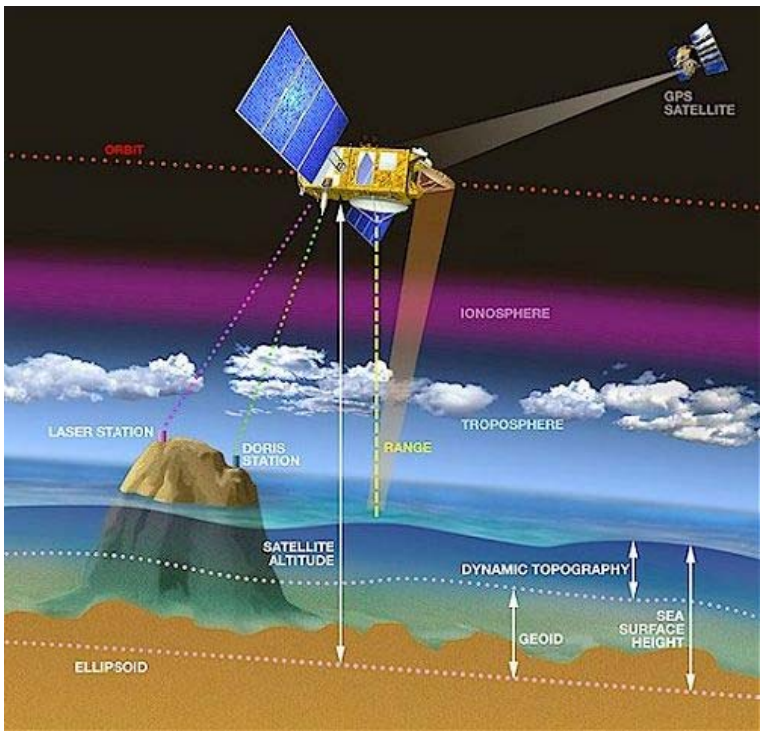

Figure 3.1 The geometry of satellite altimetry (Courtesy of AVISO)

The satellite altitude can be obtained by a number of tracking techniques aboard the satellite, such as DORIS, SLR, PRARE and GPS. The range from the satellite to the sea surface is measured by multiplying the speed of light with a half of the two-way travel time of the radar/laser pulse transmitted from the altimeter antenna and reflected back by the sea surface.

Excluding the tidal fluctuations and sea level variations due to effects such as changes of solar heating, pressure, and wind, the instantaneous sea surface height h_{ssh} is the sum of the geoid undulation N between the geoid and the reference ellipsoid, and the dynamic sea surface topography (DSST) which is also called ocean dynamic topography (ODT). DSST consists of the mean dynamic ocean topography and the time-varying dynamic ocean topography. The mean dynamic ocean topography, also called sea surface topography (SST) (Calman, 1987), is the difference between the mean sea surface and the geoid, and caused by different salinity of the ocean waters, large-scale differences in atmospheric pressure and strong currents. It can reach 1 to 2 meters, which makes it impossible to approximate the geoid by the mean sea level if an accuracy of better than 2 meters is required (Seeber, 1993).

3.1.2 Corrections to altimeter measurements

The relation expressed in (3.1) is only good for the ideal case since we assume that there is no error in both the satellite orbits and the altimeter range measurements. But in reality, due to the inaccuracy in the models which are applied in the orbit determination, such as the gravity model and all kinds of perturbation models, and the errors in various tracking systems, the satellite altitude must be corrected to remove the effect of any orbit errors before it is used to derive the sea surface height. Here we will not discuss the orbit errors and assume h_{orb} is the satellite altitude with orbit errors adequately small for tide modeling.

The range h_{alt} in (3.1) ought to be the actual range from the satellite altimeter to the instantaneous sea surface. Three major kinds of corrections should be applied to the altimeter measurements in order to obtain accurate SSH from the satellite altimetry. The three categories of corrections are generally classified as instrument corrections, media propagation corrections, and geophysical corrections.

(1) Instrument corrections:

Instrument corrections belong to the system biases which include Doppler-shift error, center-of-mass offset, nadir error, sea state bias, time tag biases and some internal calibration biases. Generally, the overall effect of the instrumental errors can be determined and controlled in the altimeter calibration over precisely surveyed test areas (i.e. “ground truth”).

Doppler-shift error is due to the frequency Doppler shift caused by the radial velocity of the satellite. It will affect the time delay measurement, thus the range.

Center-of-mass offset will account for the difference between the phase center of the satellite antenna, where the radar pulse is transmitted and its reflection from the sea surface is received, and the mass center of the satellite on which the orbit computation is based.

Nadir error is due to the deviation of the beam direction from the vertical; thus, the range measurement results in a slant-range to a point offset from the nadir.

The sea-state bias correction compensates for the bias of the altimeter range measurement toward the troughs of the ocean waves. It is thought to arise from three interrelated effects: tracker bias, skewness bias, and electromagnetic (EM) bias. Sometimes, the sea-state bias together with the following media corrections and geophysical corrections are categorized as environmental corrections.

(2) Media corrections:

Media corrections are due to the propagation error while the radar pulse passes through the atmosphere. As shown in Figure 3.1, the pulse has to go through the

ionosphere and troposphere before it reaches the sea surface. So the media corrections include the ionosphere correction, dry-troposphere correction and wet-troposphere correction.

The ionosphere correction is frequency dependent. In the frequency domain of 14GHz, the effect of the ionosphere correction is about 5cm to 20cm, depending on the level of ionization (Lorell et al.,1982). Generally it is corrected with dual-frequency measurements such as those from the dual-frequency altimeter aboard TOPEX.

The dry-troposphere correction is due to the dry-air component in the troposphere. Since it cannot be measured directly by sensors aboard altimetry satellites, it is usually corrected by certain models such as the model by Saastamoinen (1972).

The wet-troposphere correction is due to the water vapor content in the troposphere. Compared with the dry part, it is usually worse modeled. But since the wet-troposphere correction can be measured by the microwave radiometer loaded on the altimetry satellite, it can be computed by some algorithm (Tapley et al., 1982).

(3) Geophysical corrections:

Geophysical corrections include various tide effects (solid earth tide, ocean tide, ocean loading tide, pole tide) and the inverted barometer (IB) effect which describes the ocean surface deformation due to the atmospheric loading. In general, 1 millibar increase in atmospheric pressure will result in 1 cm decrease in the ocean surface height (Ponte et al., 1991; Dorandeu and Le Traon, 1999).

The solid earth tide correction accounts for the periodic variations in sea surface height due to the deformation of the underlying non-rigid earth under the attraction of the astronomical bodies (Moon and Sun). It can be derived from the tide generating potential introduced in Chapter 2 using the so-called Love numbers. Detailed information can be found in IERS Conventions (2000) and the papers by Cartwright et al.'s papers (1971, 1973).

Ocean tides account for a significant part of the variable deformation of the sea surface. The effect of ocean tides can be computed from some available tide models, which will be introduced in section 3.2.

Ocean tides cause a temporal variation of the ocean mass distribution and the associated load on the crust, and produce time-varying deformations of the earth, which is called ocean loading tide effect. Like the solid earth tide, the displacement of the earth crust caused by ocean loading tides can be derived from the tide-generating potential (IERS Conventions (2000); Cartwright and Tayler, 1971; Cartwright and Edden, 1973). Schwiderski (1980) proposed the 7% rule for ocean loading tides, which means, as an approximation, the ocean loading tide height is about 7% of the corresponding ocean tide height.

The pole tide is generated by the centrifugal effect of polar motion. Its effect can be computed if the location of the pole as a function of the polar motion angles is known (Wahr, 1985).

Considering all of the above corrections to the altimeter range, we can rewrite (3.1) as

$$\begin{aligned} h_{ssh} &= h_{orb} - h_{alt} \\ &= h_{ssh}^{obs} - h_{instr} - h_{ssb} - h_{iono} - h_{dry} - h_{wet} - h_{sol} - h_{oc} - h_{ol} - h_{pole} - h_{IB} - e \\ &= h_{ssh}^{corr} - (h_{oc} + h_{ol}) - e \end{aligned} \tag{3.2}$$

where h_{instr} is the instrument correction, h_{ssb} is the sea state bias correction, h_{iono} is the ionosphere correction, h_{dry} is the dry-troposphere correction, h_{wet} is the wet-troposphere correction, h_{sol} is the solid earth tide correction, h_{oc} is the ocean tide correction, h_{ol} is the ocean loading tide correction, h_{pole} is the pole tide correction, h_{IB} is the inverted barometer correction, and e denotes the observational noise.

Actually, depending on the subjects, the media and geophysical corrections can be regarded as signals of interest as well. If the altimeter observations are used in the determination of the geoid, all of these should be treated as corrections and be removed from the observations. But in ocean tide modeling, the ocean tide effect is the signal we are interested in, thus it should not be treated as a correction to the observations but as signal contained in the observations.

3.2 Ocean tide modeling

Based on (3.1) and (3.2), after correcting for the instrument correction and for the environmental corrections except for the ocean tide and ocean loading tide corrections, the instantaneous sea surface height h_{ssh}^{corr} from satellite altimetry can be expressed as

$$h_{ssh}^{corr} = N + DSST + h_{otide} + e \tag{3.3}$$

where N denotes the geoid undulation and $DSST$ the dynamic sea surface topography; furthermore, h_{otide} includes the effects from both ocean tide h_{oc} and ocean loading tide h_{ol} stated above. In some literature, h_{otide} is named as elastic ocean tidal height or geocentric tidal height which is used to compute the correction to altimetry; h_{oc} is named as pure ocean tidal height which is consistent with the tide gauge measurements

and measured from the ocean bottom. So we have

$$h_{otide} = h_{oc} + h_{ol} \tag{3.4}$$

As stated in Chapter 1, satellite altimetry brought the revolution in the study of ocean tides. It became possible to derive a global ocean tide model from satellite altimetry based on the expression (3.3) and the tidal analysis methods introduced in Chapter 2. In general, three kinds of methods for ocean tide modeling are applied to develop ocean tide models. In this section, some representative global ocean tide models with their revised versions (if applicable) will be briefly reviewed based on their methodologies.

3.2.1 Hydrodynamic models

Due to the impossibility to get an analytical solution of the LTE, numerical methods have long been the objective way to model ocean tides. Hydrodynamic models are derived by solving the LTE and using bathymetry data as boundary conditions. In hydrodynamic numerical modeling, the dissipation caused by bottom friction is critical. It is commonly admitted that the bottom friction is very weak in the deep ocean, but is the major contributor to the tidal energy budget over the continental shelves and shallow water seas where tidal currents are amplified. Some models have treated this problem by using linear or quadratic parameterization of bottom friction and including the shallow areas in their domain of integration, some other models by assuming the ocean as frictionless but allowing energy to radiate through boundaries with the shallow water areas where energy is dissipated. An advantage of numerical models is the introduction of solid earth tides, ocean tide loading and self-attraction into the dynamic equations. But the weakness in hydrodynamic models is their inadequacy to correctly simulate energy dissipation. One way to overcome this weakness is to increase the resolution, and another way is to use the finite element method which improves the modeling of rapid changes in ocean depth, the refinement of the grid in shallow waters and the description of the irregularities of the coastlines (Le Provost, 2001).

Two hydrodynamic models are described in this section. The first one is Schwiderski's model. It was developed by Schwiderski (1980), who constructed the hydrodynamic interpolation scheme to include the dataset of tidal constants derived from a global collection of tide gauge data in the integration of the LTE. Although this model depended on the quality of the observations used and is now known to contain some large errors, it had been used as the best available model for more than a decade. With a resolution of $1^o \times 1^o$, Schwiderski's model covers the world ocean, except for some semi-enclosed basins like the Mediterranean. A total of 11 tidal constituents is included in the model: 4 semidiurnal (M_2, S_2, N_2, K_2), 4 diurnal (K_1, O_1, P_1, Q_1) and 3 long periods (S_{sa}, M_m, M_f).

The second model is the FES94.1 model, which was developed by Le Provost et al. (1994). This model is based on the nonlinear barotropic shallow water equations, initially

formulated by Le Provost and Vincent (1986), with bottom friction parameterized through a quadratic dependency on local tidal velocities and through tidal forcing derived from astronomical potential, and including solid earth tides, ocean tide loading, and self attraction. The equations were numerically solved by the finite element method. The FES94.1 model is "purely hydrodynamic", fully independent of any measurement data. It provides a resolution of $0.5^o \times 0.5^o$, and has a full coverage of the world ocean, including marginal seas and high latitudes, especially areas covered by ice and under permanent ice shelves in the Weddel Sea and the Ross Sea, which makes it the default solution in some T/P-derived models for the region beyond $\pm 66^o$ (e.g., CSR4.0, GOT99.2b), but this model is undefined in the Mediterranean sea. The FES94.1 model includes 13 constituents: 8 major constituents (M_2, S_2, N_2, K_2, $2N_2$, K_1, O_1, Q_1) obtained from simulation, and 5 secondary constituents (Mu_2, Nu_2, L_2, T_2, P_1) deduced by admittance along with nodal modulations and equilibrium long period tides.

3.2.2 Empirical models

Empirical ocean tide models own their success to the high precision satellite altimeter measurements. They are derived by extracting ocean tide signals from the satellite altimetry. The empirical ocean tide models describe the total geocentric ocean tides, which include the effects of ocean loading. Thus, those models can be used directly in altimetry applications (e.g. for ocean tide corrections). In general, there are two ways to produce models: direct analysis of altimetry data, and direct analysis of altimetry residual. In the first method, a full tide solution is derived by analyzing the sea surface height (SSH) derived from altimetry without applying the correction with an *a priori* ocean tide model. In the second method, the SSH is preliminary corrected for the effect of ocean tides with an *a priori* ocean tide model; then the SSH residuals after the *a priori* ocean tide correction are analyzed to derive the "residual tide solution", which is actually considered as correction to the *a priori* model and can be added to the *a priori* model to get the new full model. However, the second approach does not fulfill the requirements of a rigorous adjustment as it is executed in two steps.

The first altimetry-derived model was given by Cartwright and Ray (1990, 1991) based on the analysis of 2.5 years of Geosat altimetry data through the orthotide formalism. Since the launch of ERS-1 in 1991, and especially since the launch of T/P in 1992, more than 20 global tide models have been developed from altimetry data. Considering the limit of content, only three empirical ocean tide models will be described as an illustration of this kind of models.

The DW95 model is a purely empirical ocean tide model developed by Desai and Wahr (1995, 1997). The present version 7.0 is estimated from the observations that were collected during the repeat cycles 10-229 of the T/P altimeter mission. The orthotide response formalism is used to represent the diurnal and semidiurnal ocean tides, while a constant admittance is assumed across narrow bandwidths around each of the monthly

(M_m), fortnightly (M_f), and termensual (M_t) tidal components. This model is the most exclusively empirical one with no reference to any *a priori* tide model and no direct or indirect information from the dynamics of tides. The tide solution is estimated in bins of size 2.834^o in longitude by 1^o in latitude and then smoothed to 1^o by 1^o grids within the limit of the T/P spatial coverage of $\pm 66^o$. Beyond $\pm 66^o$, this model is extended with the Schwiderski ocean tide model.

The CSR4.0 model is the revision of the older version CSR3.0 by Eanes and Bettadpur (1995). The CSR ocean tide model series has been developed using T/P altimetry data and the orthotide method. The CSR4.0 model is obtained by the analysis of about 6.4 years of T/P altimetry data, which were used to solve for corrections to CSR3.0. The FES94.1 model is the underlying reference model for CSR3.0, where corrections were produced in $3^o \times 3^o$ spatial bins and then smoothed by convolution with a 2-d Gaussian for an output on a $0.5^o \times 0.5^o$ grid.

The GOT99.2b model is an updated version of the model developed at the NASA-GSFC, known as SR94 (Schrama and Ray, 1994), SR95.0/.1, etc. 232 cycles of T/P altimetry data were used to derive the solution for 8 major semidiurnal and diurnal tides (Q_1, O_1, P_1, K_1, N_2, M_2, S_2, K_2). The tides were computed as adjustments to the FES94.1 model, and outside the latitude limit of the T/P data ($\pm 66^o$) the model defaults to FES94.1. The latest version of the GOT model series is GOT00.2. Here, 286 cycles of T/P data were used, which were supplemented in shallow seas and in polar seas by 81 35-day cycles of ERS-1/2 data in the assimilation process. Also the *a priori* models used in GOT00.2 include not only FES94.1 but some local hydrodynamic models (ftp://iliad.gsfc.nasa.gov/ray/GOT00.2). As a result, GOT00.2 is different from FES94.1 in the polar regions. The tide solutions are given on a $0.5^o \times 0.5^o$ grid.

3.2.3 Assimilation models

In contrast to the hydrodynamic modeling of ocean tides, the empirical approach does not require the knowledge of either bathymetry or coast geometry, nor some other complicated assumptions upon the dissipation laws, the bottom friction coefficient, and how to solve the hydrodynamic equations. However, the weakness of satellite altimetry, coming from the aliasing problem (which will be introduced in Chapter 4) due to the sampling period of the satellite altimeter, the limit of spatial coverage, and the spatial sampling resolution, has brought up some questions in the altimetry-derived empirical models (e.g., the relatively poor accuracy in the coastal regions where data are sparse). While, on the other hand, the numerical nature of hydrodynamic modeling makes it possible to design the resolution of the models as high as desired, provided that the computer capacity permits it. But the hydrodynamic models always exhibit the potential of inaccuracy arising from inadequate bathymetry data and unknown friction and viscosity parameters (Ray et al., 1996), which especially affect the modeling of shallow water tides. So here comes the third modeling method, named assimilation method,

which solves the hydrodynamic equations with altimetric and tide gauge data assimilation. In this section, three tide models are reviewed as examples for these assimilation models.

The NAO.99b is a global ocean tide model developed by Matsumoto et al. (2000). It uses the hydrodynamic tidal equations derived by Schwiderski (1980), and the tide solution is estimated on a $0.5^o \times 0.5^o$ grid by assimilating about 5 years of T/P altimeter data into the barotropic hydrodynamic model. The response method with orthotide formulation is applied to analyze the residual sea surface heights. The free core nutation (FCN) resonance effect and the radiational potential are included through slight modification of the standard orthotide method.

The TPXO.6.2 model is the current version of the global tidal solution developed by Egbert et al. (1994, 2002) using the inverse scheme OTIS (Oregon State University Tidal Inversion Software) to assimilate observation data to the hydrodynamic equations by a representer approach. The tides are provided as complex amplitudes of earth-relative sea-surface elevation for eight primary (M_2, S_2, N_2, K_2, K_1, O_1, P_1, Q_1) and two long-period (M_f, M_m) harmonic constituents on a $0.25^o \times 0.25^o$ full global grid.

The FES99 model is an improvement over its predecessor FES98 (Lefèvre et al., 2000) which only included tide gauge data in the assimilation, but no altimetry data. In FES99, approximately 700 tide gauges and 687 T/P altimetric crossover datasets were assimilated by a revised representer assimilation method to improve the accuracy of FES98. For both models, the solutions are distributed on a $0.25^o \times 0.25^o$ global grid. The latest version of the FES model series is FES2004, which is the last update of the FES2002 solution.

CHAPTER 4

TIDAL ALIASING

4.1 Introduction to tidal aliasing in satellite altimetry

Based on the sampling theorem, to reconstruct the original analog signal, it is necessary to sample the signal at a rate higher than twice the highest frequency v in the signal, i.e. $f_N = 2v$, where f_N is called Nyquist frequency. In terms of periods, a time-continuous signal of period T_w can be fully reconstructed from its sampled values if the samples are taken over at least T_w at an interval of less than $T_w/2$. However, if the sampling interval exceeds $T_w/2$, the signal of period T_w will be aliased to a longer period T_a, which is called aliased period.

For an altimeter satellite in a repeat orbit with a period of *P* days, the altimeter samples the tide at a given point on the groundtrack once every *P* days. Since in general, the repeat period *P* of an altimeter satellite is a few days or more, e.g. for T/P, $P = 9.9156$ days, for ERS-1/2, $P = 35$ days, for GEOSAT/GFO, $P = 17.0505$ days, the diurnal and semidiurnal tides are always aliased to long period signals by the periodic sampling of the satellite altimeter. This is the inherent problem in satellite altimetry and causes the difficulty in the separation of tide constituents when trying to extract tide signals from altimetry data using harmonic analysis.

For a tide constituent of frequency f_k, its aliased frequency f_a can be calculated by (Yuchan Yi, personal communication)

$$f_a = \left| \mathrm{mod}(f_k + \frac{f_s}{2}, f_s) - \frac{f_s}{2} \right| \tag{4.1}$$

where $f_s = 1/P$ is the sampling frequency of the satellite altimeter. For M_2, its original frequency is 1.9305 cycles per day, so its aliased frequency sampled by T/P is 0.0161 cycles per day, the corresponding aliased period of which is 62.107 days. Table 4.1 lists the aliased periods of the major diurnal and semidiurnal tide constituents sampled by T/P, ERS-1/2 and GEOSAT/GFO. From the table, it can be seen that the period of K_1 is aliased to 173.192 days by T/P which is close to the period of the semiannual signal, and

aliased to 365.242 days by ERS-1/2 which is the same as the aliased period of P_1 by ERS-1/2 and the period of the annual signal. Especially, because of the sun-synchronous orbit of ERS-1/2, S_2 is aliased to infinite period.

According to the Rayleigh criterion, in order to separate two neighboring tides which have nearly the same angular frequencies w_1 and w_2, the minimum time span of the data which should be analyzed is determined by

$$T_r \left| w_1 - w_2 \right| \geq 2\pi \tag{4.2}$$

where T_r is known as Rayleigh period, and can be calculated by

$$\frac{1}{T_r} = \left| \frac{1}{T_1} - \frac{1}{T_2} \right| \tag{4.3}$$

with $T_1 = 2\pi / w_1$, $T_2 = 2\pi / w_2$. So, for T/P, all the major tides with the aliased periods listed in Table 4.1, can be resolved and separated by using 3 years of T/P data except that the separation of K_1 from S_{sa} can only be obtained by the use of 9 years worth of data. For ERS-1/2 and GEOSAT/GFO, since the aliased periods and the Rayleigh periods are generally much larger, it means that more data are needed to obtain reliable tidal estimates from ERS-1/2 and GEOSAT/GFO altimetry. For example, 9 years of ERS-1/2 data are required to separate M_2 and N_2, and since M_2 is aliased to 317 days by GEOSAT/GFO, which is close to the period of the annual signal, it is difficult to separate M_2 from the annual signal from less than 6 years of data (see Table 4.1, Smith, 1999).

Tide Constituent	True Period (days)	Aliased Period (days)		
		Sampled by T/P ($P = 9.9$ days)	Sampled by ERS-1/2 ($P = 35$ days)	Sampled by GEOSAT/GFO ($P = 17$ days)
M_2	0.518	62.107	94.486	317.108
S_2	0.5	58.742	∞	168.817
N_2	0.527	49.528	97.393	52.072
K_2	0.499	86.596	182.621	87.724
K_1	0.997	173.192	365.242	175.448
O_1	1.076	45.714	75.067	112.954
P_1	1.003	88.891	365.242	4466.665
Q_1	1.120	69.365	132.806	74.050

Table 4.1 Aliased periods of major tide constituents sampled by three altimetry satellites

To decorrelate the aliased tides, Smith (1999) proposed two methods in his dissertation, using phase advance differences from adjacent groundtracks and crossing groundtracks. In this study, we investigate the possible improvement of extracting ocean tide signals from altimeter data at crossover points by frequency analysis based on a global optimization and an interval method.

4.2 Study of tidal aliasing in satellite altimetry based on frequency analysis

Periodic sampling of the altimetry satellite causes the aliasing of short period tides, which makes it difficult to extract the tide signals using harmonic analysis with single satellite altimetry data due to the correlation of aliased tides and the demand of long data series to decorrelate the tides. In this section, an effort to investigate the feasibility of improving the tidal aliasing problem based on frequency analysis is described, using simulated along-track altimetry data and altimetry data at crossovers.

4.2.1 Global optimization method

Global optimization can be based on a global search method which may be used for spectral analysis of a time series with unknown frequencies. Compared with spectral analysis using Fourier series, in which the frequencies are chosen beforehand and are not necessarily based on the physical reality, or on *a priori* physical knowledge, the global approach allows one to find the physically meaningful frequencies more accurately and to describe the data with fewer parameters (Mautz, 2002).

Global search is based on the idea to evaluate the objective function at various points and to determine the global minimum according to certain decision criteria. Let us assume that the model function

$$f(t) = \sum_{k=1}^{m} a_k \sin(2\pi f_k t + \varphi_k) \tag{4.4}$$

consists of m superimposed harmonic functions and is a qualified description for the time series $y(t)$, where a_k is the amplitude, φ_k is the (initial) phase, and f_k is the frequency. To find the unknown frequencies in the time series, we construct the objective function:

$$Q(a_k, \varphi_k, f_k) = \sum_{i=1}^{n} \left(f(t_i) - y(t_i) \right)^2 = \sum_{i=1}^{n} \left(\sum_{k=1}^{m} a_k \sin(2\pi f_k t_i + \varphi_k) - y(t_i) \right)^2 \tag{4.5}$$

which is minimized at certain values for a_k, φ_k, and f_k. To apply a global method to the optimization problem (4.5), we rewrite (4.5) into

$$Q = \sum_{i=1}^{n} e_i^2 = F(f_1, \cdots, f_m; a_1, ..., a_m; \varphi_1, ..., \varphi_m)$$

$$= F(f_1, ..., f_m; A_1, ..., A_m; B_1, ..., B_m) \tag{4.6}$$

with

$$\begin{aligned} -e_i &= \sum_{k=1}^{m} A_k \sin(2\pi f_k t_i) + \sum_{k=1}^{m} B_k \cos(2\pi f_k t_i) - y(t_i) \\ A_k &= a_k \cos\varphi_k \\ B_k &= a_k \sin\varphi_k \end{aligned} \tag{4.7}$$

The primary procedure of finding the global minimum of (4.6) is to construct values for the frequencies within the interval $[0, \cdots, n/2]$, n is the number of observations. A random search procedure is applied which is advantageous, due to the robustness towards special properties of the objective function. Then A_k, B_k and finally Q are calculated. By calculating several values of Q at various points, the optimal set of frequencies, which makes Q globally minimum, can be found through a sophisticated iteration process (Mautz, 1999).

The above global optimization procedure is equally applicable to any observation models that also contain non-periodic parts such as polynomial terms, which lead to:

$$-e_i = a_0 + a_1 t_i + a_2 t_i^2 + \cdots + \sum_{k=1}^{m} A_k \sin(2\pi f_k t_i) + \sum_{k=1}^{m} B_k \cos(2\pi f_k t_i) - y(t_i) \tag{4.8}$$

4.2.1.1 Numerical experiments using simulated along-track altimetry data

To validate the software of the global optimization method in searching tidal frequencies in altimetry data, which are affected by the aliasing problem, we applied the frequency analysis based on the global optimization to simulated T/P and ERS altimetry data and compared it to the results of least squares procedure with known frequencies.

First, simulated time series sampled by T/P, ERS and GFO are generated using given amplitudes/phases and true frequencies of major diurnal and semidiurnal tides and an annual signal. Tables 4.2, 4.3 and 4.4 show the results from frequency analysis using the global optimization method, where the frequencies are estimated along with amplitudes and phases. From the results, it can be seen that the amplitudes and aliased tidal periods due to the periodic sampling of the altimeters are almost exactly identified using the global optimization approach. But there are some problems in getting the original phases back that were used in generating the simulated time series.

For simulated time series sampled by the T/P repeat period, only the phases of M_2 and O_1 are recovered correctly; the phases of other major short period tides are different from the given values by the sign.

	Period (days)			Amplitude (cm)		Phase (degree)	
	True period	Aliased period		Given value	Estimated value	Given value	Estimated value
		Theoretical value	Estimated value				
M_2	0.518	62.107	62.107	16.6	16.6	-8	**-8**
S_2	0.5	58.742	58.742	5.0	5.0	-22	22
N_2	0.527	49.528	49.528	4.0	4.0	7	-7
K_2	0.499	86.596	86.596	1.4	1.4	-20	20
K_1	0.997	173.192	173.192	11.1	11.1	-49	49
O_1	1.076	45.714	45.714	10.9	10.9	-45	**-45**
P_1	1.003	88.891	88.891	3.8	3.8	-44	44
Q_1	1.120	69.365	69.364	2.6	2.6	-81	81
Annual signal	365.242	365.242	365.242	8.5	8.5	0	0

Table 4.2 Frequency analysis of a simulated time series sampled by the T/P repeat period

As stated before, the aliased period of S_2 by the ERS sampling rate is infinity, which makes it impossible to extract S_2 from harmonic analysis, since it may have merged into the constant term as bias. This is also true for the frequency analysis in our study, where S_2 cannot be identified although the original frequency of S_2 is included in the simulated time series sampled by the ERS repeat period. Also, since the periods of both K_1 and P_1 are aliased to an annual period, the same as that of the annual signal, these three components cannot be separated by the frequency analysis using the global optimization approach. In addition, contrary to the case displayed in Table 4.2, the phase estimates in Table 4.3 are problematic for M_2 and O_1, whereas in Table 4.2 only the estimated phases for M_2 and O_1 are identified correctly.

	Period (days)			Amplitude (cm)		Phase (degree)	
	True period	Aliased period		Given value	Estimated value	Given value	Estimated value
		Theoretical value	Estimated value				
M_2	0.518	94.486	94.487	16.6	16.6	-8	**8**
S_2	0.5	∞	-	5.0	-	-22	-
N_2	0.527	97.393	97.393	4.0	4.0	7	7
K_2	0.499	182.621	182.621	1.4	1.4	-20	-20
K_1	0.997	365.242	365.243	11.1	19.384	-49	-17.2
O_1	1.076	75.067	75.067	10.9	10.9	-45	**45**
P_1	1.003	365.242	-	3.8	-	-44	-
Q_1	1.120	132.806	132.806	2.6	2.6	-81	-81
Annual signal	365.242	365.242	-	8.5	-	0	-

Table 4.3 Frequency analysis of a simulated time series
sampled by the ERS repeat period

The same problem appeared in the case displayed in Table 4.4 where, based on the global optimization procedure, the phase estimates for M_2 and O_1 are problematic which were derived from the simulated time series sampled by the GFO repeat period.

To further validate the results from the frequency analysis using global optimization which searches for unknown frequencies, a least squares procedure with known frequencies is applied to the above three simulated along-track time series. As for the global optimization procedure, there is no problem in amplitude estimation from the least squares procedure. The phase estimates from the least squares procedure are listed in Table 4.5, where two cases are considered. The first case (I) used the true original tidal frequencies as known frequencies and gave out correct phase estimates from the least squares procedure. The second case (II) used the aliased tidal frequencies as known frequencies, and the same problems for phase estimates appeared as seen in Tables 4.2, 4.3 and 4.4.

	Period (days)			Amplitude (cm)		Phase (degree)	
	True period	Aliased period		Given value	Estimated value	Given value	Estimated value
		Theoretical value	Estimated value				
M_2	0.518	317.108	317.109	16.6	16.6	-8	**8**
S_2	0.5	168.817	168.817	5.0	5.0	-22	-22
N_2	0.527	52.072	52.072	4.0	4.0	7	7
K_2	0.499	87.724	87.724	1.4	1.4	-20	-20
K_1	0.997	175.448	175.448	11.1	11.1	-49	-49
O_1	1.076	112.954	112.954	10.9	10.9	-45	**45**
P_1	1.003	4466.665	4466.664	3.8	3.8	-44	-44
Q_1	1.120	74.050	74.050	2.6	2.6	-81	-81
Annual signal	365.242	365.242	365.243	8.5	8.5	0	0

Table 4.4 Frequency analysis of a simulated time series
sampled by the GFO repeat period

These results show that, due to the altimeter sampling, the tidal signals along track are aliased tidal signals, and the results from the global optimization procedure are correct, as they are consistent with the result from the least squares approach with the aliased frequencies as known frequencies. It shows that aliased tidal periods have some effect on the correct extraction of phase information from the along-track altimetry data.

	Sampled by T/P		Sampled by ERS		Sampled by GFO	
	Phase estimates (I)	Phase estimates (II)	Phase estimates (I)	Phase estimates (II)	Phase estimates (I)	Phase estimates (II)
M_2	-8	**-8**	-8	**8**	-8	**8**
S_2	-22	22	-	-	-22	-22
N_2	7	-7	7	7	7	7
K_2	-20	20	-20	-20	-20	-20
K_1	-49	49	-17.2	-17.2	-49	-49
O_1	-45	**-45**	-45	**45**	-45	**45**
P_1	-44	44	-	-	-44	-44
Q_1	-81	81	-81	-81	-81	-81
Annual signal	2.66e-7	2.66e-7	-	-	1.76e-6	1.76e-6

Table 4.5 Phase estimates from the least squares procedure using known frequencies

4.2.1.2 Numerical experiments using simulated ERS data at single satellite crossovers

At single satellite crossovers, the sampling rate by satellite altimeters does not change significantly, neither do the aliased tidal periods (Andersen, 1994). But due to the characteristics of crossovers, which are the intersections of ascending and descending tracks, twice the observations are available at crossovers.

Let us assume 1.389 days delay between ERS ascending and descending tracks; simulated time series of ERS altimetry data at one single satellite crossover are generated without noise included. Now we apply the global optimization method to the simulated data, and it is found that aliased periods, although not exactly identical with the theoretical values, are obtained. Table 4.6 displays the results from the globally optimal frequency searching procedure.

	Estimated period (days)	Estimated amplitude (cm)	Estimated phase (degree)
M_2	93.66	9.43	63.86
S_2	-	-	-
N_2	97.70	1.12	-21.26
K_2	181.96	1.06	-50.86
K_1	362.09	13.28	3.21
O_1	74.49	6.09	-7.24
P_1	-	-	-
Q_1	131.65	1.95	-38.64
Annual signal	-	-	-

Table 4.6 Frequency analysis of a simulated time series
at ERS single satellite crossovers (no Gaussian noise is assumed)

Similar least squares procedures using true original frequencies (I) and aliased frequencies (II) as known frequencies are tested, respectively. The results are listed in Table 4.7. Comparing the results in Table 4.6 and 4.7, it can be seen that the global optimization approach leads to estimated amplitudes which are comparable with those from the least squares procedure using known aliased frequencies; but the phase estimates end up being much different from each other, especially for N_2 (-21.26^o from the global optimization approach versus -61.23^o from the least squares procedure with known aliased frequencies). Also, when compared with the given amplitudes and phases used in the generation of the simulated data, the estimated amplitudes and phases deviate much from the given values. For example, for M_2, the given amplitude and phase are 16.6 cm and -8^o; but the estimates of amplitude and phase from the global optimization are 9.43 cm and 63.86^o, and those from the least squares procedure (II) are 9.64 cm and 62.70^o. This seems to show that neither the global optimization method, nor the least squares method is a good enough tool to extract tidal signals from altimetry data at single satellite crossovers, although the least squares method with true original frequencies as known frequencies performs better than the two others.

	Amplitude (cm)			Phase (degree)		
	Given value	Estimated value (I)	Estimated value (II)	Given value	Estimated value (I)	Estimated value (II)
M_2	16.6	16.65	9.64	-8	-7.67	62.70
S_2	5.0	-	-	-22	-	-
N_2	4.0	3.99	1.36	7	5.50	-61.23
K_2	1.4	1.56	1.04	-20	-35.86	-60.43
K_1	11.1	11.97	13.28	-49	-45.11	3.59
O_1	10.9	11.10	6.17	-45	-44.82	-10.58
P_1	3.8	-	-	-44	-	-
Q_1	2.6	2.73	1.95	-81	-78.72	-37.92
Annual signal	8.5	-	-	0	-	-

Table 4.7 Estimates of amplitudes and phases from the least squares procedure

4.2.2 Interval method

Due to the poor performance of the global optimization method in frequency analysis of simulated time series at single satellite crossovers, we applied an interval method, which is another kind of frequency search method (Rainer Mautz, personal communication). The basic idea of the interval method is described in the following with the same model function and objective function as for the global optimization method.

For equally spaced data, a discrete set of orthogonal frequencies f_i is given by

$$f_i = \frac{j}{\Delta t_{total}} = \frac{j}{t_n - t_1} \tag{4.9}$$

where $j = 1,2,\cdots,N$, $N = \frac{n-1}{2}$; t_1 is the first observation time, t_n is the last observation time, and n is the number of observations. The Nyquist frequency f_N is determined by

$$f_N = \frac{N}{\Delta t_{total}} \tag{4.10}$$

and the aliased frequency of the original frequency f is given by

$$f_a = \pm \left| f - 2mf_N \right| \tag{4.11}$$

where *m* are positive integers.

As an example, for a time series with $n = 185$ and $\Delta t_{total} = 1824.47$ days, we have $f_N = 0.0504$ cycles per day, which is the maximum frequency that can be detected from the time series. For the M_2 tide with $f = 1.9323$ cycles per day, we have $f_a = 0.0161$ cycles per day with $m = 19$. So f_a is in the detectable frequency interval [0, f_N], but f is beyond the detectable frequency interval. However, since the frequency spectrum repeats after [0, f_N], by applying an interval method, which searches for frequencies interval by interval (which explains the name of this method), we can go beyond the limit of [0, f_N] and get the real, non-aliased frequency with additional information such as long data series, which provides the minimum Q (Rainer Mautz, personal communication). For the M_2 tide, it is 1.9323 cycles per day with $m = 0$. So, the interval method seems to better identify the true signals in the time series, no matter what the sampling rate is.

For unequally spaced data, such as the combined time series sampled at multiple rates, the interval method is still applicable, and the true frequencies can be detected.

The interval method is applied to the simulated altimetry time series at T/P single satellite crossover and T/P_ERS dual satellite crossover. It is interesting to find that, when there is no noise assumed for the simulated time series, the true original frequencies along with the given amplitudes and phases can be accurately identified with the interval method for time series at single satellite crossover. If Gaussian noise is assumed, 4 tidal components (S_2, N_2, K_2, Q_1) cannot be accurately extracted when using time series at T/P single satellite crossover, 3 tidal components (P_1, K_2, Q_1) cannot be accurately extracted when using time series at T/P_ERS dual satellite crossover. Especially, S_2 and N_2 can be better identified from data at dual satellite crossover than from data at single satellite crossover. To save space, only the results where noise is assumed, which are certainly more realistic for actual altimetry data, are listed in Table 4.8 and 4.9. All of the outputs from the programs are attached in the Appendix A, where the phase output should be transformed via the following relation:

$$phase = \frac{p \times 180^\circ}{\pi} - 90^\circ \tag{4.12}$$

The results in Table 4.8 and 4.9 show that appropriate harmonic analysis with single and dual satellite crossover data can accurately identify true, non-aliased frequencies and corresponding amplitudes and phases for dominant tides. The estimates of amplitudes are better than those of phases, the largest error in the phase estimate reaches up to 177.087^o and 174.737^o for Q_1 in two tables, and the corresponding vector differences are 5.09 cm and 5.72 cm, respectively. The vector difference here is defined as the root sum of squared differences in cosine and sine amplitudes, i.e. $\sqrt{\Delta h_1^2 + \Delta h_2^2}$, where Δh_1 is the cosine amplitude difference between true and estimated values, Δh_2 is the sine amplitude difference.

	Frequency (cycles/day)		Amplitude (cm)		Phase (degree)		Vector difference (cm)
	True value	Estimated value	Given value	Estimated value	Given value	Estimated value	
M_2	1.932274	1.932273	16.6	16.78	-8	-8.017	0.18
S_2	2.000000	0.017011	5.0	5.09	-22	25.399	4.06
N_2	1.895982	1.432113	4.0	3.86	7	-10.440	1.20
K_2	2.005476	0.616650	1.4	1.04	-20	18.849	0.88
K_1	1.002738	1.002734	11.1	11.44	-49	-48.384	0.36
O_1	0.929536	0.929538	10.9	11.06	-45	-46.224	0.28
P_1	0.997262	0.997243	3.8	3.81	-44	-32.314	0.78
Q_1	0.893244	0.417808	2.6	2.49	-81	96.087	5.09
Annual signal	0.002738	0.002737	8.5	8.42	0	-0.308	0.09

Table 4.8 Frequency analysis at T/P single satellite crossovers using the interval method (Gaussian noise of 3 cm is assumed)

	Frequency (cycles/day)		Amplitude (cm)		Phase (degree)		Vector difference (cm)
	True value	Estimated value	Given value	Estimated value	Given value	Estimated value	
M_2	1.932274	1.932279	16.6	16.62	-8	-10.158	0.63
S_2	2.000000	2.000010	5.0	5.21	-22	-25.847	0.40
N_2	1.895982	1.895984	4.0	4.04	7	9.974	0.21
K_2	2.005476	1.339448	1.4	1.40	-20	221.464	2.41
K_1	1.002738	1.002737	11.1	11.03	-49	-48.566	0.11
O_1	0.929536	0.929541	10.9	11.14	-45	-46.437	0.37
P_1	0.997262	0.291314	3.8	3.75	-44	-48.273	0.29
Q_1	0.893244	0.316966	2.6	3.13	-81	93.737	5.72
Annual signal	0.002738	0.002731	8.5	8.50	0	7.458	1.11

Table 4.9 Frequency analysis at T/P_ERS dual satellite crossovers using the interval method (Gaussian noise of 3 cm is assumed for T/P data and 8 cm for ERS data)

Due to the better performance of the interval method with simulated time series at dual satellite crossovers, we use this interval method to extract major tidal signals from actual altimetry data at TOPEX_ERS-2 dual satellite crossovers. The altimetry data at several crossovers are used and the results are attached in Appendix B. The results show that some of the dominant tidal constituents (M_2, S_2, N_2, K_1, P_1, O_1) can be identified from the frequency analysis of actual altimetry data at dual satellite crossovers.

4.3 Summary

Tidal aliasing is caused by the periodic sampling of satellite altimeters. The aliased information is inherent in along-track altimetry data. Based on the above numerical experiment with simulated and actual altimetry data, we can see that it is possible to extract the original ocean tide signals by use of altimetry data at crossover locations with a proper analysis method. In our experiments, the software for the interval method performs better than that for the global optimization method in recovering the ocean tide signals with altimetry data at crossovers in spite of the existence of tidal aliasing. Also since at crossover locations, much denser altimetry data are available than at along-track locations, this provides a possible basis for our later ocean tide modeling effort using various altimetry data at crossovers.

CHAPTER 5

OCEAN TIDE MODELING IN THE SOUTHERN OCEAN

Ocean tides play a significant role in the complex interactions between solid earth, ocean, sea ice, and floating glacial ice shelves. Tidal currents create a turbulent mixing at the bottom of an ice shelf, contributing to the creation of rifts for the possible detachment of parts of icebergs, and tides can influence heat transport between the ice shelf and sea water (Robertson et al., 1998). Tides near and under floating ice shelves and sea ice influence grounding line locations and, depending on surface and basal slopes, grounding lines migrate with time within a grounding zone (Rignot, 1998; Metzig et al., 2000). Improved knowledge of grounding lines is inherently necessary to study the ice mass balance and its contribution to the global sea level change.

A number of global ocean tide models have been developed since the launch of the T/P satellite altimeter. Those models have achieved an accuracy of $\pm$(2-3 cm) in deep oceans (Shum et al., 1997, 2001), but they are much less accurate in coastal seas (Shum et al., 2001). In addition, ocean tide models are largely unreliable in parts of the polar oceans which are covered by permanent or seasonal sea ice and which are beyond the geographical coverage of the T/P satellite altimeter. In this chapter, we first present an evaluation of the performance of current tide models in the Southern Ocean, and then an empirical ocean tide solution for the area below -50^o in latitude is presented using the orthotide formulation; its performance is evaluated by intercomparison with several other tide models.

5.1 Accuracy assessment of ocean tide models in the Southern Ocean

Global ocean tide models have been very accurate in deep oceans, but their performance in the polar areas which are beyond the T/P satellite altimeter coverage is constrained by hydrodynamic models such as FES94.1. For the tides in the polar areas, several studies have been carried out, including tide studies in the Weddell Sea and Ross Sea in Antarctic (Robertson et al., 1998; Rignot et al., 2000; Padman et al., 1998, 1999, 2002, 2003; Fricker and Padman, 2002) and tide studies in the Arctic ocean (Kowalik and Proshutinsky, 1994; Padman and Erofeeva, 2004). In this section, two global models (GOT99.2b, NAO.99b) and one regional model (CATS02.01) are evaluated by their performance in the Southern Ocean which is below -50^o in latitude.

The CATS02.01 (hereafter CATS) model is a Circum-Antarctic Tidal Simulation model developed by L. Padman (personal communication). It is a 10-constituents model (M_2, S_2, N_2, K_2, O_1, K_1, P_1, Q_1 and M_m, M_f) on a $1/4 \times 1/12$ degree (lon.$\times$lat.) grid of

resolution, covering the area from -58^o to -86^o in latitude. It uses linear drag parameterization, which leads to a better agreement with the Antarctic tide height data than the earlier CATS01.02 which was based on quadratic drag. GOT99.2b (hereafter GOT) and NAO99.b (hereafter NAO) are both global models with $0.5^o \times 0.5^o$ resolution. They have been introduced in Chapter 3.

The evaluation is based on the intercomparison of the above three models using the *RMS* deviation of the amplitude of each tidal constituent, sea surface height residual analysis and comparison with available "ground truth", such as tide gauge and gravimetric data.

To compare two models, the inphase and quadrature terms (see definition in Chapter 2) of each constituent from a tide model are computed and compared in terms of the *RMS* deviation of amplitude defined as follows:

$$RMS = \sqrt{\frac{1}{2N}\sum_{i=1}^{N}\left\{\left[h_1^a(i) - h_1^b(i)\right]^2 + \left[h_2^a(i) - h_2^b(i)\right]^2\right\}} \tag{5.1}$$

where h_1, h_2 are inphase and quadrature terms, and superscripts a, b stand for two different models. N is the total number of locations where h_1 and h_2 are computed.

In the comparison, the major diurnal constituents (K_1, O_1, P_1, Q_1) and semidiurnal constituents (M_2, S_2, N_2, K_2) are included. To account for the total effect of 8 major constituents, we define *RSS* (root sum of squares) as

$$RSS = \sqrt{\sum_{j=1}^{8} RMS(j)^2} \tag{5.2}$$

where j is the index for the 8 tidal constituents stated above, and *RMS* is defined in (5.1) for each tidal constituent.

Table 5.1 illustrates the *RMS* deviation between each pair of the three models in the Southern Ocean. From the table, we can see M_2, S_2 and K_1 have the largest differences between paired models. And the differences between the CATS model and the GOT model as well as the difference between the CATS model and the NAO model are smaller than the difference between the NAO model and the GOT model for all the major constituents except for Q_1. The *RMS* deviation of M_2 between the NAO and the GOT models is ± 8.74 cm, the largest among all the differences listed in Table 5.1.

	K_1	O_1	P_1	Q_1	M_2	N_2	K_2	S_2
CATS-GOT	3.31	3.67	1.02	0.68	3.42	1.62	1.13	3.40
CATS-NAO	3.58	3.01	1.28	0.87	7.97	1.45	1.55	5.01
NAO-GOT	4.41	4.01	1.43	0.82	8.74	1.83	1.66	5.42

Table 5.1 Comparison of tide models in the Southern Ocean
in terms of *RMS* deviations (unit: ± cm)

To display the geographical distribution of the difference between the models, for each paired models, the *RSS* for the 8 major constituents are computed according to (5.2) at each model grid point and then the obtained *RSS*'s are averaged over the three pairs. The final difference distribution between models in terms of *RSS* for the South Ross Sea area is shown in Figure 5.1. The distribution shows that the difference becomes larger towards the south pole, and the largest difference between models occurred in the glacial ice shelf covered oceans which is as large as ± 30 cm (and more).

Ocean tides are a major factor for the sea surface height variation. Using the altimetry sea level data opens another way to evaluate the performance of ocean tide models. Since geocentric ocean tides should be used for altimetry data and the CATS model only provides the pure ocean tides, the ocean loading tides derived from the NAO model are added to the pure ocean tides from the CATS model to obtain the required geocentric tides for the CATS model. 9 years of T/P and 6 years of ERS-2 altimetry sea level data below -50^o are used in the study to investigate the performance of the different tide models in terms of the sea level residual after correcting the tide effects using different models. The T/P and ERS-2 along-track data used in this study have been generated from the altimetry Stackfiles (Yuchan Yi, personal communication). The comparison of the studied three models is shown in Table 5.2.

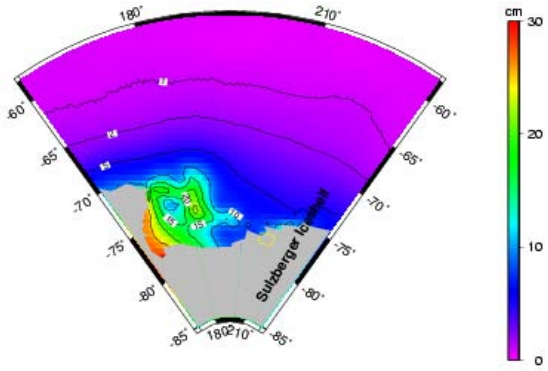

Figure 5.1 Combined model difference in the Ross Sea area

	NAO.99b	GOT99.2b	CATS02.01
T/P (10/24/1992-12/06/2001)	29.1 ± 9.7	29.1 ± 9.7	28.5 ± 10.2
ERS-2 (05/16/1995-01/08/2001)	31.7 ± 21.6	31.6 ± 21.7	31.0 ± 22.0

Table 5.2 Model validation with altimeter sea level data of T/P and ERS-2 below 50S (mean difference ± standard deviation in cm)

From Table 5.2, the NAO and GOT models provide almost the same magnitude of the residuals, with a standard deviation of ± 9.7 cm for T/P and ± 21.6 cm for ERS-2. The CATS model has slightly larger standard deviation of ± 10.2 cm for T/P altimetry residuals and ± 22.0 cm for ERS-2 altimetry residuals.

"Ground truth" data are often used to validate tide models. The tide harmonics derived from those "ground truth" data, such as tide gauge and gravimeter results, are compared with those from the tide models. Here, in Table 5.3, the three tide models are compared with the gravimeter result (Williams and Robinson, 1980) at Little America V (~ 78.2S, 197.73E) using the individual *RMS* deviations and the *RSS* as defined in (5.1) and (5.2). Since only 6 tidal constituents have been analyzed from the gravimeter result, *RSS* is the total effect of these 6 constituents. The comparison results show that that CATS02.01 model agrees best with the gravimeter data at Little America with an *RSS* of

$\pm$9.7 cm. Also, the K_1 and O_1 constituents of the three models show the largest differences from the gravimeter data.

Tide Model	K_1	O_1	P_1	M_2	N_2	S_2	*RSS*
NAO.99b	10.4	6.5	3.3	1.7	1.8	0.6	13.0
GOT99.2b	6.4	4.7	2.3	4.4	2.9	2.6	10.1
CATS02.01	6.0	6.3	2.0	1.9	2.2	2.6	9.7

Table 5.3 Tidal comparison at Little America V (unit: $\pm$ cm)

Tide gauge data are another form of independent “ground truth” data, which allow us to validate the tide models. Figure 5.2 shows the distribution of the 102 pelagic tide gauges (denoted by inverted triangles) and 739 coastal tide gauges (denoted by circles) obtained from Richard D. Ray (1999, personal communication), where red symbols denote those gauges below -60^o.

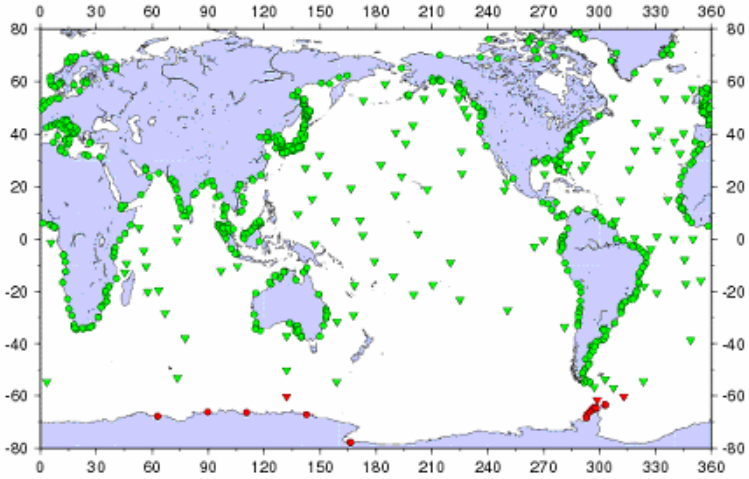

Figure 5.2 Distribution of tide gauges

Table 5.4 and 5.5 show the comparison of the individual *RMS* deviations and the *RSS* between the tide models and the tidal harmonics derived from tide gauge data below -60^o. Due to the latitude limitation, only 3 pelagic tide gauges and 12 coastal tide gauges below -60^o are available. The comparison results show that the GOT model performs best when compared with pelagic or coastal tide gauges, and the CATS model is a little worse than

the other two models when compared with pelagic tide gauges; the NAO model is the worst when compared with coastal tide gauges. But since at some coastal tide gauges the tide models have no definition, which results in a different number of locations included in each tide model, and since also some tidal harmonics were not derived from some tide gauge records, the comparison with the coastal tide gauges seems not to provide appropriate information about the performance of the tide models. The numbers in the parentheses in Table 5.5 denote the number of tide gauges which have those tidal harmonics. For example, for K_1, 11 tide gauges have this tidal harmonics and can be interpolated from the NAO model, but only 1 tide gauge can be interpolated from the GOT model, and 7 tide gauges can be interpolated from the CATS model.

Tide Model	K_1	O_1	P_1	Q_1	M_2	N_2	K_2	S_2	*RSS*
NAO.99b	1.46	1.01	0.43	0.55	1.90	0.36	0.38	0.99	2.92
GOT99.2b	1.36	0.82	0.27	0.41	1.43	0.24	0.43	1.09	2.50
CATS02.01	1.11	0.92	0.29	0.51	2.12	0.44	0.37	1.29	2.99

Table 5.4 Comparison of tide models with pelagic tide gauges
below -60 degree (unit: ± cm)

Tide Model	K_1	O_1	P_1	Q_1	M_2	N_2	K_2	S_2	*RSS*
NAO.99b	11.36 (11)	11.77 (11)	3.36 (9)	2.21 (4)	6.53 (12)	2.45 (9)	1.71 (10)	5.44 (12)	19.10
GOT99.2b	4.55 (1)	6.10 (1)	1.08 (1)	1.13 (1)	2.70 (1)	0.73 (1)	0.84 (1)	3.61 (1)	9.05
CATS02.01	4.13 (7)	8.31 (7)	1.49 (7)	1.07 (2)	6.11 (7)	2.66 (7)	1.69 (7)	6.23 (7)	13.25

Table 5.5 Comparison of tide models with coastal tide gauges
below -60 degree (unit: ± cm)

5.2 Empirical tide modeling in the Southern Ocean

Tides are major causes of time-dependent ice shelf elevation variations. Removal of tides from the remote sensing measurements of ice shelf surface elevation changes and the study of ice motion require accurate tidal prediction models. Recent global models are

constrained to fit T/P data, which are limited within $\pm 66^{o}$ latitude. However, ERS-1/2 and Geosat/GFO satellite altimeters have more extended spatial coverage than T/P; these provide a possible source of data that can be used in tide modeling, especially for the area beyond T/P coverage. In this study, a modified orthotide formulation is applied to analyze the T/P and ERS-2 altimetry data at dual satellite crossover locations and single satellite crossover locations to obtain a point-wise empirical tide solution for the Southern Ocean below -50^{o}.

5.2.1 Data

Crossovers are those locations where the ascending and descending tracks of the altimeter satellites intersect. Due to the tidal aliasing resulting from the altimeter periodic sampling and due to the relatively sparse track spacing of the T/P satellite, we choose to use the T/P and ERS-2 altimetry data at crossover locations for tidal analysis. There are several advantages to use altimetry data at crossovers: At single satellite crossovers, although the aliasing period is not changed, the number of observations can double if compared to along-track data (Andersen, 1994); at dual satellite crossovers, due to the different sampling rate of two satellites, the aliasing problem can be dampened.

In this study, three groups of datasets at crossover locations are generated from the altimetry Stackfile (Yuchan Yi, personal communication). Except for ocean tide and ocean loading tide corrections, the general corrections to these altimetry data, which are introduced in Chapter 3, have been applied to the Stackfile data. These three groups of datasets at crossovers are TOPEX altimetry data at TOPEX single satellite crossovers, ERS-2 altimetry data at ERS-2 single satellite crossovers, and altimetry data from TOPEX and ERS-2 at TOPEX_ERS-2 dual satellite crossovers. The TOPEX and ERS-2 Stackfile data used to generate these datasets for tide modeling in the Southern Ocean are summarized in Table 5.6 (no POSEIDON data are used in this study).

Altimeter	Cycles	Latitude coverage (^{o})	Longitude coverage (^{o})
TOPEX	4-364	-50 ~ -66	0 ~ 360
ERS-2	1-79	-50 ~ -81.5	0 ~ 360

Table 5.6 Altimetry data used for tide modeling in the Southern Ocean

5.2.2 Empirical tide modeling using an orthotide formulation

Response methods have been extensively used in tide modeling because of their advantage when deriving a solution for any constituent from a relatively few parameters. These few parameters are used to describe the supposedly smooth admittance function within each tidal band. To evade the tidal aliasing problem, somewhat described in Chapter 4, we adopted the orthotide formalism as proposed by Groves and Reynolds (1975) for our empirical tide modeling in the Southern Ocean. Since no *a priori* tide models have been applied in the corrections to the altimetry data we used, the ocean tidal solution we obtained is the full geocentric tidal solution. A modification to the orthotide formalism, which includes annual, semiannual, monthly and fortnight tide components in harmonic forms, was made in our study.

Considering the major diurnal and semidiurnal tidal bands and the stated 4 long-period tides, the sea surface height (SSH) $\zeta(\lambda,\varphi,t)$, which contains the total effect of pure ocean tides and ocean loading tides, is described using the extended orthotide formulation as follows:

$$\zeta(\lambda,\varphi,t) = \sum_{m=1}^{2}\sum_{k=0}^{2}\left[u_{mk}(\lambda,\varphi)P_{mk}(t) + v_{mk}(\lambda,\varphi)Q_{mk}(t)\right] + \sum_{i}\left[a_{i1}(\lambda,\varphi)\cos(w_i t) + a_{i2}(\lambda,\varphi)\sin(w_i t)\right] + bias + noise \qquad (5.3)$$

where $P_{mk}(t)$ and $Q_{mk}(t)$ are orthotide functions, which can be determined by the tide generating potential; u_{mk} and v_{mk} are the location-dependent orthoweights, which will be solved for together with the cosine and sine amplitudes a_{i1} and a_{i2} for the four long-period tides (S_a, S_{sa}, M_m and M_f). In (5.3), w_i are the frequencies of the four long-period tides, respectively. For each satellite altimeter, a bias term is evaluated together with the tide components. So, for a tide solution using altimetry data at single satellite crossovers, there are 21 unknowns in (5.3), and for a tide solution using altimetry data at dual satellite crossovers, there are 22 unknowns.

We write (5.3) in a general linear observation model as $Y = AX + e.$ The incorporation of *a priori* information can be treated in two ways as stated by Jackson (1979). In a general way, the *a priori* information can be treated in form of "pseudo-observations" explicitly, thus we have

$$\begin{aligned} Y &= AX + e \\ X_0 &= X + e_0 \end{aligned} \qquad (5.4)$$

where Y is the $n \times 1$ observation vector, X is the $m \times 1$ unknown parameter vector, A is the $n \times m$ coefficient matrix, $e \sim N(0, C_e)$ is the random observation error, X_0 is the *a priori* vector for X, $e_0 \sim N(0, C_X)$ is the random error vector of the *a priori* information and $COV(e, e_0) = 0$. Then an estimate of X is given by (Jackson, 1979)

$$\hat{X} = (A^T C_e^{-1} A + C_X^{-1})^{-1} (A^T C_e^{-1} Y + C_X^{-1} X_0) \tag{5.5}$$

If the unknown parameters are treated as Gaussian random variables with given mean X_0 and dispersion matrix C_X (Jackson, 1979), the prediction of X is also given by (5.5), which, in the special case of $X_0 = 0$ (Jackson, 1979), reduces to:

$$\hat{X} = (A^T C_e^{-1} A + C_X^{-1})^{-1} A^T C_e^{-1} Y \tag{5.6}$$

In this study, we assume C_e and C_X to be diagonal. The *a priori* accuracy of ± 3 cm for T/P altimetry data and ± 8 cm for ERS-2 altimetry data are specified based on the empirical accuracy of altimetry data. For T/P data, 100^2 cm^2 is used on the diagonal of C_X, and for ERS-2 data, 1000 cm^2 is used on the diagonal of C_X (Andersen, personal communication). Also, a value of 1000 cm^2 is used as the diagonal values of C_X when both T/P and ERS-2 altimetry data at dual satellite crossover locations are used.

The ocean tide solutions we derived are point-wise solutions, this means that for each location, a solution was obtained by adjusting (5.3) using formula (5.6) and a group of observation data at that location. Considering the iteration process used in the least squares procedure where the weights are updated based on residuals, the weights applied to the observations are different from location to location. This approach is denoted as different weights in the following section.

For comparison, least squares procedures using one common weight, one value which is used for the observational data at all locations, are also carried out to get the full tide solution. The first case is to use the *a priori* accuracy (± 3 cm for T/P, ± 8 cm for ERS-2, both squared) as common weight for the observations of the respective altimeters, and the second case is to use the accuracy estimates derived from the different weighting procedures as common weights for the observations of the respective altimeters. These two approaches are denoted as constant weight I and constant weight II.

5.2.3 Tide solutions and their evaluation

Point-wise empirical tide solutions have been obtained based on the above extended orthotide formulation and the respective weighting methods. Using the three groups of datasets introduced in 5.2.1, tide solutions at three groups of crossover locations have been obtained respectively. To validate the tide modeling procedure and to evaluate the obtained tide solutions, the point-wise solutions are compared with three other models regarding their performance in reducing the standard deviation (hereafter STD) of the SSH residuals after the ocean tide correction, and in terms of the individual *RMS* deviations and the *RSS* of the tide constituents.

The three other models used in the evaluation are summarized in Table 5.7, in which the ocean loading tide from NAO.99b (NAO) is added to the CATS02.01 (CATS) model so that the CATS model can be applied to the altimetry data.

Model	Coverage	Resolution (lat×lon)	Constituents	Tide constituents Grid provided
NAO.99b	90S-90N 0-360	$0.5^{o} \times 0.5^{o}$	8 major, 16 minor, long period	geocentric tide, pure ocean tide, ocean loading tide
TPXO.6.2	90S-90N 0-360	$0.25^{o} \times 0.25^{o}$	8 major, Mm, Mf	geocentric tide, pure ocean tide
CATS02.01	58S-86S 180W-180E	$1/12^{o} \times 1/4^{o}$	8 major, Mm, Mf	pure ocean tide
Note	8 major means the 8 major diurnal and semidiurnal tide constituents			

Table 5.7 Summary of the tide models used in this evaluation

First, the efficiencies of three weighting methods are evaluated. When using three weighting methods, three sets of tide solutions are obtained. Their performances in reducing the STD of the SSH residuals are compared with each other. Table 5.8 lists the comparison between the three weighting methods when TOPEX and ERS-2 data at the dual satellite crossovers are used to obtain the tide solution at dual satellite crossovers. Considering later comparisons with other models which do not include annual tide, the tide component inseparable from the annual signal due to the ocean thermo effect, we define SSH residuals here as

$$\text{SSH residuals} = \text{SSH} - (\text{diurnal} + \text{semidiurnal tides}) - \text{LP} \tag{5.7}$$

The effects of diurnal and semidiurnal tides are obtained from our solution, and the equilibrium long-period tides, LP, are calculated using the subroutine written by Cartwright (adopted from the GOT99.2b model).

If TOPEX data are considered to evaluate the performance of the tide solution, the tide solution using the first weighting method in Table 5.8 gives the smallest STD of the SSH residuals ($\pm$8.98 cm). But if considering the reduction of the STD of the SSH residuals for ERS-2 data, the second weighting method in Table 5.8 performs best ($\pm$ 12.73 cm). For both cases, the use of different weights shows the second-best performance. The minor change in values for the TOPEX data seem to suggest that the weighting method does not affect the result for TOPEX data too much, which is also evidenced by the result in Table 5.9.

SSH Data at TOPEX/ERS-2 dual satellite crossovers	No. of locations	Constant weight I (Topex: $\pm$3 cm ERS-2: $\pm$8 cm)	Constant weight II (Topex: $\pm$9 cm ERS-2: $\pm$12 cm)	Different weights
TOPEX data	21408	8.98	9.01	9.00
ERS-2 data	21408	12.92	12.73	12.77

Table 5.8 STD of the SSH residuals at dual satellite crossovers below -50^o
(where tidal effects are corrected using respective tide solutions, unit: $\pm$ cm)

Intercomparison of the NAO model, the TPXO.6.2 (TPXO) model and the CATS model with the above mentioned three sets of tide solutions using data at dual satellite crossovers are also carried out to evaluate the efficiency of the alternative weighting methods. Table 5.9 lists the comparison results in terms of the *RSS* defined in (5.2). The results show that the use of different weights gives the smallest *RSS*, no matter whether compared with the NAO model (*RSS* = $\pm$ 2.16 cm), the TPXO model (*RSS* = $\pm$ 2.24 cm), or the CATS model (*RSS* =$\pm$ 2.34 cm). The bottom two rows in Table 5.9 show the effect of the weighting methods on the tide solutions when using data at single satellite crossovers. It is interesting to find that the tide solution using TOPEX data at single satellite crossovers was almost not affected by the weights applied to the data, which is shown by an identical *RSS*, no matter which kind of weighting method is applied. Considering the comparison result related to the three weighting methods, we prefer the use of different weights. Therefore, in the following discussion, we concentrate on the evaluation of the tide solutions obtained by using the different weights.

	Constant weight I			Constant weight II			Different weights		
	NAO	TPXO	CATS	NAO	TPXO	CATS	NAO	TPXO	CATS
Topex/ERS-2 data at dual satellite crossovers	2.22	2.30	2.38	2.22	2.29	2.41	**2.16**	**2.24**	**2.34**
Topex data at single satellite crossovers	1.72	1.81	1.98	1.72	1.81	1.98	1.72	1.81	1.98
ERS-2 data at single satellite crossovers	11.66	11.67	14.53	10.89	10.89	13.58	**10.47**	**10.48**	**12.98**

Table 5.9 Intercomparison of tide solutions using three weighting methods with selected models in terms of *RSS* (unit: ± cm)

To compare our solution with other tide models, we use the three models in Table 5.7 to predict geocentric tidal height at the dual satellite crossovers, then apply the tidal height to correct the SSH at dual satellite crossovers; thus we get the SSH residuals after tidal corrections from the tide models. Table 5.10 lists the comparison between the tide models and our tidal solution at dual satellite crossovers, using different weights in terms of the STD of the SSH residuals.

SSH Data at TOPEX/ERS-2 dual satellite crossovers	STD of SSH before tidal correction	STD of SSH residuals after tidal correction (± cm)			
		Solution of our study	NAO99	TPXO.6.2	CATS02.01
TOPEX data	20.55	8.27 (13518)	8.51 (13518)	8.68 (13505)	9.13 (13389)
ERS-2 data	23.30	13.57 (13518)	13.69 (13518)	13.77 (13505)	14.21 (13389)

Note: Numbers in parentheses stand for the valid number of locations included in the calculation, where tide solutions are available from the model

Table 5.10 STD of the SSH residuals after tidal correction
(dual satellite crossovers, latitude: < -58^o)

As in Table 5.8, two cases are considered in this comparison. Since the CATS model is only valid for the area from -58^o to -86^o, the comparison region is constrained to below -58^o instead of -50^o. Define the tidal power as STD_a^2-STD_b^2, where subscript a and b denote the results from two tidal corrections, we can say that the tidal power of our solution over the NAO model is 2.0^2 cm^2, the tidal power over the TPXO model is 2.6^2 cm^2, and the tidal power over the CATS model is 3.9^2 cm^2, if considering TOPEX data. For ERS-2 data, the tidal powers are 1.8^2 cm^2, 2.3^2 cm^2 and 4.2^2 cm^2, respectively.

To illustrate the spatial distribution of the difference demonstrated in Table 5.10, the STD of the SSH residuals are plotted in Figure 5.3 and 5.4 for TOPEX data and in Figure 5.5 and 5.6 for ERS-2 data. However, due to the small differences between models, the figures don not show the detail of the differences very clearly. In Figure 5.7, the differences between the two figures (left – right) from Figure 5.3 are plotted to show that the differences are less than 0.2 cm with a maximum of 0.12 cm and a minimum of -5.03 cm; at most locations, they are negative. Similarly for ERS-2 data, in Figure 5.8, the differences between the two figures (left – right) from Figure 5.5 are plotted and the difference has a maximum of 1.49 cm and a minimum of -2.28 cm, with most of them being less than zero. Both the comparison results in Table 5.10 and the plots of the differences show that our tide solution performs a little better than the other three models in reducing the STD of the SSH residuals. However, we should mention that the good performance of our solution is an *internal* agreement because those altimetry data have already been used in the least squares procedure for the tide solution. Therefore, it is recommended to use some other independent data to validate the performance of our solutions with respect to other models. Also, because of the difference among tide models in those tide constituents included in the tidal height calculation, the small differences of the STD of the SSH are reasonable.

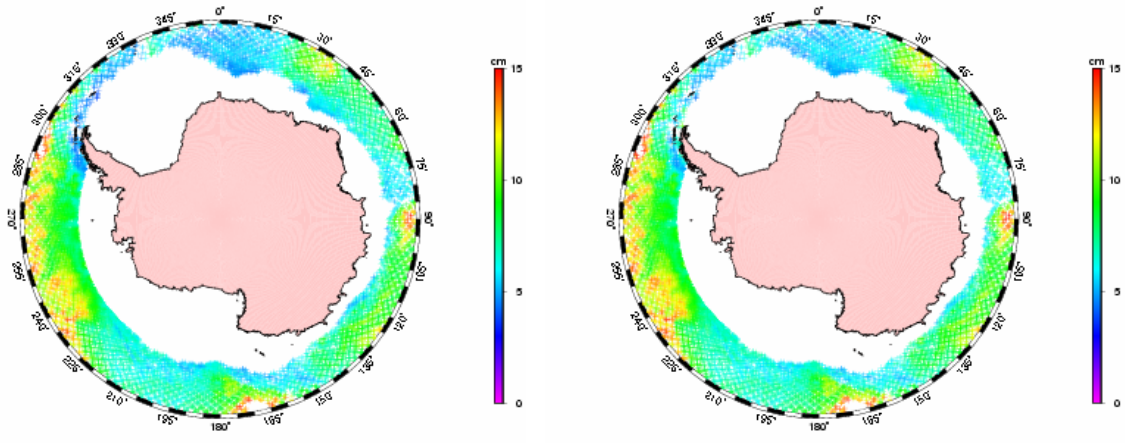

Figure 5.3 Standard deviation of the SSH residuals for TOPEX data (latitude: < -58^{o})
(left: this study, right: NAO99 tide model)

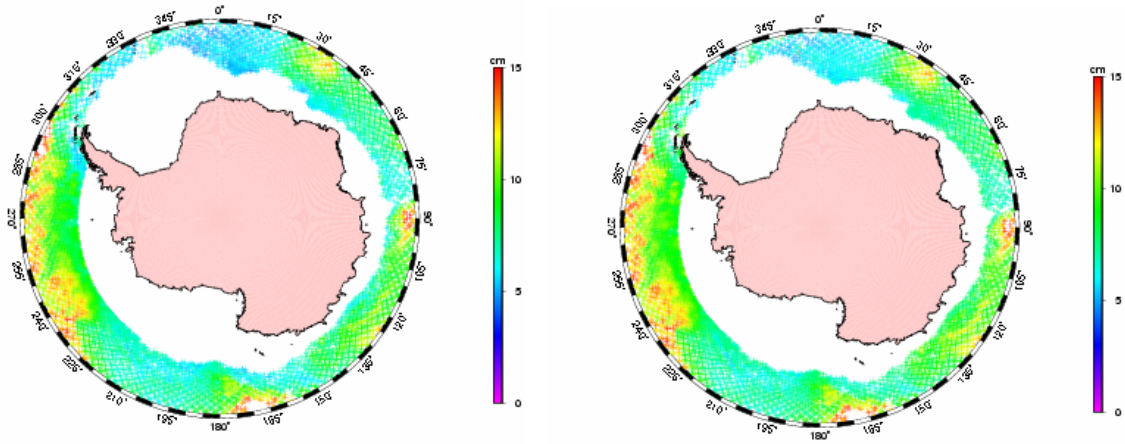

Figure 5.4 Standard deviation of the SSH residuals for TOPEX data (latitude: <-58^{o})
(left: TPXO.6.2 tide model, right: CATS02.01 tide model)

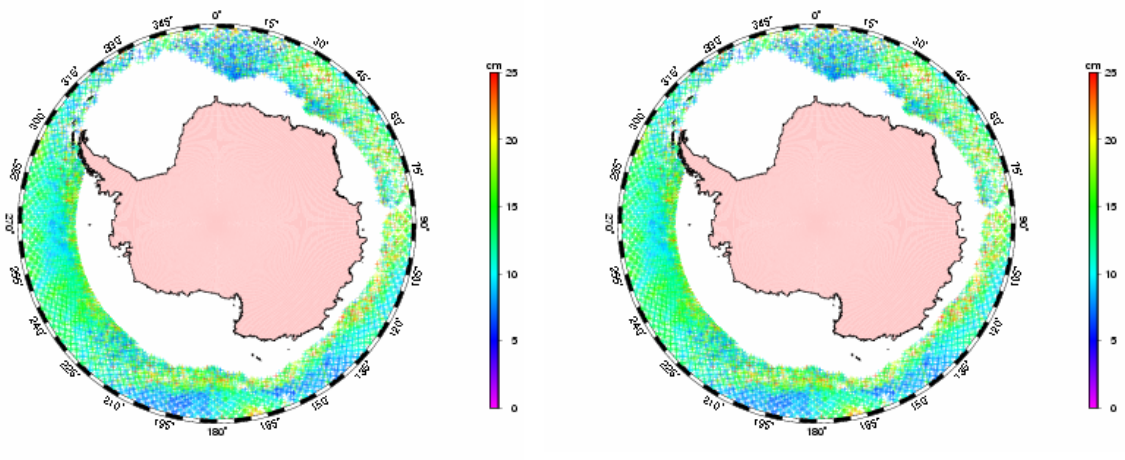

Figure 5.5 Standard deviation of the SSH residuals for ERS-2 data (latitude: <-58^{o})
(left: this study, right: NAO99 tide model)

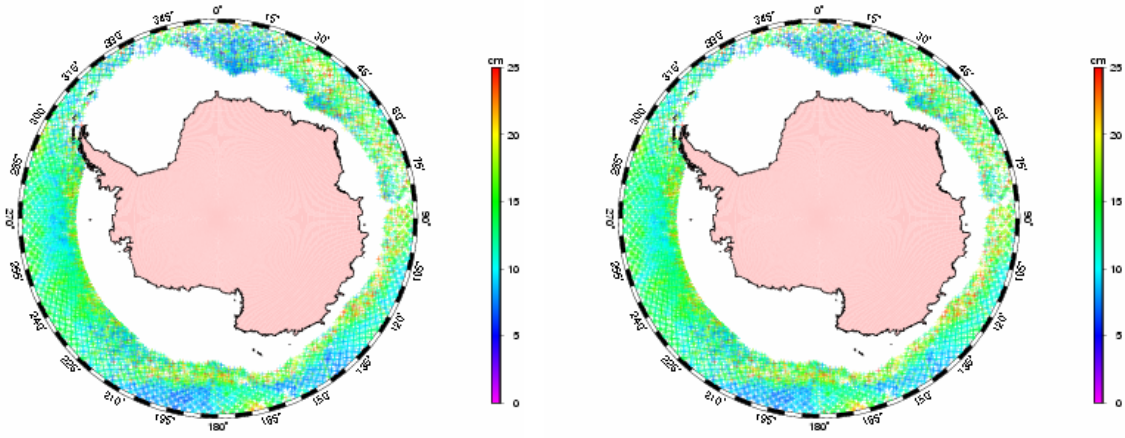

Figure 5.6 Standard deviation of the SSH residuals for ERS-2 data (latitude: <-58^{o})
(left: TPXO.6.2 tide model, right: CATS02.01 tide model)

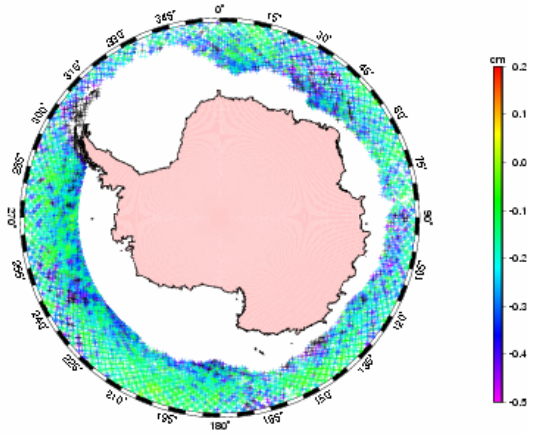

Figure 5.7 Difference between the STD of the SSH residuals for TOPEX data

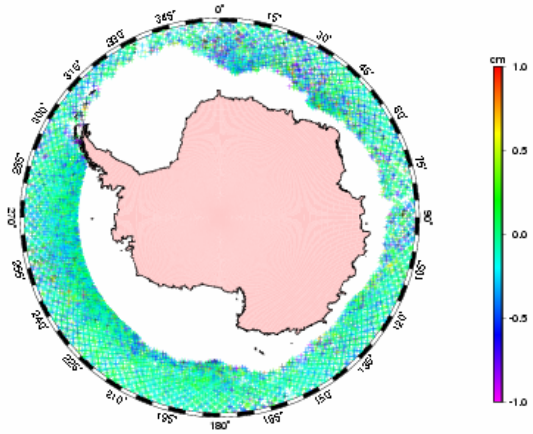

Figure 5.8 Difference between the STD of the SSH residuals for ERS-2 data

Table 5.11 shows the comparison between the NAO model, the TPXO model, the CATS model, and the tide solutions obtained by use of altimetry data at TOPEX or ERS-2 single satellite crossovers in terms of the STD of the SSH residuals. Here the tide solution of our study uses different weights.

SSH Data at single satellite crossovers	STD of SSH before tidal correction	STD of SSH residuals after tidal correction (± cm)			
		Solution of our study	NAO99	TPXO.6.2	CATS02.01
TOPEX	20.53	8.31 (2023)	8.46 (2023)	8.63 (2021)	9.09 (2020)
ERS-2	23.56	13.24 (5129)	13.95 (5129)	14.05 (5124)	14.58 (4672)

Table 5.11 STD of the SSH residuals after tidal correction
(single satellite crossovers, latitude: < -58^{o})

Comparing the number of locations in Table 5.10 and 5.11, we can see that combining ERS-2 data with TOPEX data can improve the spatial resolution of the tide solutions, which is actually attributed to the dense spatial sampling characteristics of

ERS-2 coupled with the lower orbital inclination of T/P. But due to the relatively poor accuracy of the ERS-2 data, the resulting tide solutions using TOPEX and ERS-2 data at dual satellite crossovers did not improve over the tide solutions using TOPEX data only at single satellite crossovers. That is shown in Table 5.9 (where different weights were used); for when compared with the NAO model, the tide solution using both altimeter measurements gives an *RSS* of ± 2.16 cm. It is slightly larger than the *RSS* of ± 1.72 cm when only TOPEX data are used for the tidal analysis.

Table 5.12 lists the differences between the 8 major tidal constituents from our solution (using different weights) and those from the NAO model, the TPXO model and the CATS model in terms of the *RMS* deviations defined in (5.1). Among these, the S_2 tide has the largest *RMS* deviation, and K_1 has the second-largest *RMS* deviation when intercompared with these three models. Also, the *RMS* deviation shows that our solution has slightly better agreement with the NAO model and the TPOX model than with the CATS model.

Moreover, it is obvious that the poorer accuracy of and severe aliasing problem with the ERS-2 data have significant effects on the resulting tide solutions. The tide solutions using ERS-2 data only have much larger differences. Especially for the S_2 tide, the vector differences reach up to 8.71 cm from the NAO model, 8.72 cm from the TPXO model, and 10.71 cm from the CATS model.

Since the annual signal of sea level change caused by the solar heating of the ocean water has the same frequency as the annual tide component, it is difficult to separate the annual signal from the annual tide. To demonstrate the influence of the annual terms, which may contain the annual tide component and the annual signal of sea level change, we subtract S_a obtained from our study from the SSH and compare the SSH residuals as we did for Table 5.10. The results are shown in Table 5.13.

DATA	M_2	S_2	N_2	K_2	K_1	P_1	Q_1	O_1	Model
Topex data at single satellite crossovers	0.58	**0.95**	0.46	0.19	**0.89**	0.30	0.46	0.62	NAO
	0.57	**1.06**	0.48	0.38	**0.88**	0.36	0.46	0.59	TPXO
	0.65	**1.03**	0.53	0.45	**1.06**	0.31	0.50	0.70	CATS
ERS2 data at single satellite crossovers	1.89	**8.71**	1.59	2.66	**3.59**	1.18	1.72	1.87	NAO
	1.90	**8.72**	1.60	2.65	**3.55**	1.20	1.73	1.87	TPXO
	2.18	**10.71**	1.89	3.26	**4.84**	1.56	2.00	2.22	CATS
Topex/ERS-2 data at dual satellite crossovers	0.76	**1.15**	0.61	0.28	**1.10**	0.36	0.62	0.78	NAO
	0.76	**1.25**	0.63	0.43	**1.08**	0.41	0.62	0.76	TPXO
	0.80	**1.20**	0.69	0.50	**1.20**	0.37	0.65	0.82	CATS

Table 5.12 Intercomparison of our tide solution with selected models in terms of the *RMS* deviations for 8 major tidal constituents (unit: ± cm)

SSH Data at TOPEX/ERS-2 dual satellite crossovers	STD of SSH before tidal correction	STD of SSH residuals after tidal correction (± cm)			
		Solution of our study	NAO99	TPXO.6.2	CATS02.01
TOPEX data	20.55	8.16 (13518)	8.42 (13518)	8.60 (13505)	9.05 (13389)
ERS-2 data	23.30	13.38 (13518)	13.50 (13518)	13.61 (13505)	14.05 (13389)

Table 5.13 STD of the SSH residuals (annual terms removed) after tidal correction (dual satellite crossovers, latitude: < -58^o)

Comparing the results in Table 5.10 and 5.13, we can see that the STD reduced about 0.1 cm for TOPEX data and 0.2 cm for ERS-2 data if the annual term is removed from the sea surface height. This seems to show that the annual term has a certain effect on the calculation of the SSH residuals.

CHAPTER 6

CONCLUSIONS

In this study of ocean tide modeling in the Southern Ocean, an empirical ocean tide solution was presented using an orthotide formulation and altimetry data at crossover locations. The combination of TOPEX and ERS-2 data at dual satellite crossover locations for tidal solution was investigated using the method of different weights. Compared with two other weighting methods, which assume constant weights to the altimetry data, no matter where the location is, the method of different weights gives a little better results in the ocean tide solution.

The empirical ocean tide solutions are evaluated by comparison with the NAO model, the TPXO model and the CATS model. The intercomparison shows that our empirical solution using TOPEX and ERS-2 data at dual satellite crossover locations agrees well with the selected models, with an *RSS* in the magnitude of 2 cm. The comparison in terms of the standard deviation of the SSH residuals shows that our solution is slightly better than the selected models. For TOPEX data, the standard deviation of the SSH residuals after ocean tide correction using our solution is ± 8.27 cm at 13518 dual satellite crossover locations. Compared with this, the NAO model gives ± 8.51 cm at 13518 locations, the TPXO model gives ± 8.68 cm at 13505 locations and the CATS model gives ± 9.13 cm at 13389 locations. For ERS-2 data, the corresponding values of the standard deviation are ± 13.57 cm for our solution, ± 13.69 cm for the NAO model, ± 13.77 cm for the TPXO model, and ± 14.21 cm for the CATS model.

Besides the ocean tide solution based on TOPEX and ERS-2 altimetry data at dual satellite crossover locations, two other groups of ocean tide solution are presented by use of altimetry data at TOPEX single satellite crossover locations and ERS-2 single satellite crossover locations. Due to the less accurate altimetry data from ERS-2, the tide solution by incorporating ERS-2 data to TOPEX data did not perform better than the tide solution obtained using TOPEX data only. Also, the solution using ERS-2 data only at single satellite crossover locations does not agree well with the selected models, which is shown by the *RSS* growing as large as ± 10 cm when compared with the tide constituents from selected models. This suggests a problem to tidal solutions using multiple satellite altimetry data, especially when including less accurate data. So before combining altimetry data from different satellite altimeters, a good data editing to remove those data with large errors (e.g., poor data quality due to instrument maneuvers) and using some retracked data, which enable a better correction for different instrumental, environmental and orbit errors, would be recommended.

Because of the limited spatial coverage of TOPEX, the combination of TOPEX and ERS-2 data at dual satellite crossover locations is also confined to -66^{o}. Although the

coverage of the ERS-2 altimeter can reach -81.5^{o} by its orbital characteristics, the ERS-2 altimetry data we obtained are confined to the mostly south of -70^{o} because the ocean mode was switched to ice mode when the satellite flew over the area below -70^{o}, where it is assumed to be inappropriate for ocean mode operation of altimeter. So, to some extent, the tide solution provided in this study is still relatively far away from the ice-covered ocean in the Antarctic area, even though the tidal solutions using the ERS-2 data at single satellite crossovers extend a little beyond -66^{o} latitude and near to -70^{o} latitude in some area.

The combination of ERS-2 data with TOPEX data at dual satellite crossovers improved the spatial resolution of tidal solutions. This is shown by the location numbers in Table 5.10 for dual satellite crossovers and in Table 5.11 for single satellite crossovers. Also, the combination of data from two satellite altimeters with different repeat periods provides a way to reduce tidal aliasing. The techniques used in this study for dual satellite crossovers can be applied to other combinations of high-latitude satellite altimeters to improve the geographical coverage of empirical tide solutions. For example, the combination of ERS-1/2 with GFO can extend the spatial coverage to -72^{o} latitude and at the same time, the tidal aliasing may be reduced by use of the data at dual satellite crossover locations.

With the launch of ICESat in January, 2003, accurate measurements over the ice surface at the Antarctic area would provide a promising contribution to the data that could be included in the tide modeling. GEOSAT/GFO, ERS-1/2, and ENVISAT data, can also contribute to the data source for ocean tide modeling, which all have a spatial coverage beyond -66^{o} in the Southern Ocean. How to use those data to derive an ocean tide model for the Southern Ocean beyond -66^{o} latitude is what we would do in the future.

APPENDIX A

OUTPUT FROM A FREQUENCY ANALYSIS OF SIMULATED ALTIMETRY DATA AT SINGLE/DUAL SATELLITE CROSSOVERS WITH/WITHOUT NOISE ASSUMED

(1) Topex single crossover (noise-free):

```
Frequency and Phase in data units:
fno= 1 vv=    0.0000000 f=   1.9322736160 a=16.600000 p= 1.431170
fno= 2 vv=    0.0000000 f=   1.0027379093 a=11.100000 p= 0.715585
fno= 3 vv=    0.0000000 f=   0.9295357068 a=10.900000 p= 0.785398
fno= 4 vv=    0.0000000 f=   0.0027379093 a= 8.500000 p= 1.570796
fno= 5 vv=    0.0000000 f=   2.0000000000 a= 5.000000 p= 1.186824
fno= 6 vv=    0.0000000 f=   1.8959819690 a= 4.000000 p= 1.692969
fno= 7 vv=    0.0000000 f=   0.9972620907 a= 3.800000 p= 0.802851
fno= 8 vv=    0.0000000 f=   0.8932440597 a= 2.600000 p= 0.157079
fno= 9 vv=    0.0000000 f=   2.0054758185 a= 1.400000 p= 1.221731
fno=10 vv=    0.0000000 f=   1.1061388347 a= 0.000000 p= 0.483413 m0=
0.00000
Time [sec]  : 11695600.000000 f(x) evaluations: 322961 f'(x): 85093
```

(2) Topex single crossover (Gaussian noise, std=±3cm)

```
Frequency and Phase in data units:
fno= 1 vv=  5211.8945901 f=   1.9322733362 a=16.780001 p= 1.430872
fno= 2 vv=  5211.8945901 f=   1.0027341310 a=11.436730 p= 0.726343
fno= 3 vv=  5211.8945901 f=   0.9295379345 a=11.064322 p= 0.764039
fno= 4 vv=  5211.8945901 f=   0.0027374508 a= 8.422965 p= 1.565428
fno= 5 vv=  5211.8945901 f=   0.0170114600 a= 5.086918 p= 2.014097
fno= 6 vv=  5211.8945901 f=   1.4321128113 a= 3.863072 p= 1.388586
fno= 7 vv=  5211.8945901 f=   0.9972430855 a= 3.811809 p= 1.006804
fno= 8 vv=  5211.8945901 f=   0.4178075129 a= 2.493147 p= 3.247828
fno= 9 vv=  5211.8945901 f=   0.6166498950 a= 1.043724 p= 1.899771
fno=10 vv=  5211.8945901 f=   2.1903246491 a= 0.703447 p= 4.397803 m0=
2.99509
Time [sec]  : -18681972.960000 f(x) evaluations: 639457 f'(x): 169255
```

(3) Topex_ERS dual crossover (noise-free)

```
Frequency and Phase in data units:
fno= 1 vv=   15.9211602 f=   1.9322734681 a=16.589476 p= 1.432996
fno= 2 vv=   15.9211602 f=   1.0027377221 a=11.135939 p= 0.717163
fno= 3 vv=   15.9211602 f=   0.9295357671 a=10.896686 p= 0.784696
fno= 4 vv=   15.9211602 f=   0.0027387135 a= 8.519029 p= 1.560009
fno= 5 vv=   15.9211602 f=   2.0000005610 a= 4.997541 p= 1.179313
fno= 6 vv=   15.9211602 f=   1.8959818914 a= 3.993610 p= 1.693905
fno= 7 vv=   15.9211602 f=   2.2074802237 a= 3.784328 p= 0.750106
fno= 8 vv=   15.9211602 f=   0.3170134345 a= 3.833826 p= 2.479731
fno= 9 vv=   15.9211602 f=   2.0054685056 a= 1.369663 p= 1.308259
fno=10 vv=   15.9211602 f=   0.8931276334 a= 1.455574 p= 4.650055 m0=
0.20857
Time [sec]  : 10868600.000000 f(x) evaluations: 453941 f'(x): 120114
```

(4) Topex_ERS dual crossover (Gaussian noise, std=±3cm for Topex, ±8cm for ERS)

```
Frequency and Phase in data units:
fno= 1 vv=  7807.5008916 f=   1.9322791207 a=16.618595 p= 1.393501
fno= 2 vv=  7807.5008916 f=   1.0027367748 a=11.031371 p= 0.723152
fno= 3 vv=  7807.5008916 f=   0.9295408356 a=11.140399 p= 0.760323
fno= 4 vv=  7807.5008916 f=   0.0027314763 a= 8.500846 p= 1.700957
fno= 5 vv=  7807.5008916 f=   2.0000097990 a= 5.211391 p= 1.119687
fno= 6 vv=  7807.5008916 f=   1.8959843543 a= 4.040949 p= 1.744868
fno= 7 vv=  7807.5008916 f=   0.2913142675 a= 3.747735 p= 0.728266
fno= 8 vv=  7807.5008916 f=   0.3169662288 a= 3.125893 p= 3.206809
fno= 9 vv=  7807.5008916 f=   1.3394478012 a= 1.400511 p= 5.436078
fno=10 vv=  7807.5008916 f=   0.6360388891 a= 1.300588 p= 0.759651 m0=
4.61865
Time [sec]  : 18071500.000000 f(x) evaluations: 736270 f'(x): 195125
```

APPENDIX B

OUTPUT OF A FREQUENCY ANALYSIS USING REAL ALTIMETRY DATA AT TOPEX_ERS-2 DUAL SATELLITE CROSSOVERS

Latitude: -66.148155 Longitude: 278.278389

	freqency	amplitude	phase			
1	1.9322745040	0.243175	3.183915	M2		
2	1.0027287771	0.111892	4.614719	K1		
3	0.9295598607	0.103420	6.041701	O1		
4	1.9999954180	0.080732	0.480312	S2		
5	2.2389016070	0.062814	1.739715			
6	0.9973009546	0.051486	2.913246	P1		
7	0.9220391655	0.034026	4.256537			
8	1.9161008354	0.017390	6.186920			
9	0.0004214765	0.024891	3.843082			
10	0.0084901752	0.021623	5.162586	vv=	1.3755098	m0= 0.06361

Latitude: -66.144067 Longitude: 278.988569

	freqency	amplitude	phase			
1	1.9322726598	0.247918	3.186657	M2		
2	1.0027221463	0.124900	4.852426	K1		
3	0.9295629933	0.124587	5.932807	O1		
4	0.2855504393	0.081163	4.678486			
5	1.8959872087	0.066850	6.268541	N2		
6	0.9972867398	0.057678	3.246870	P1		
7	0.8933140697	0.031409	1.438027	Q1		
8	1.7139305886	0.022634	4.796221			
9	1.5494683055	0.021300	5.867979			
10	1.7180154180	0.019893	1.566437	vv=	1.2752415	m0= 0.06226

Latitude: -66.136403 Longitude: 279.706746

	freqency	amplitude	phase	
1	1.9322692906	0.241143	3.266511	M2
2	1.0027280675	0.129110	4.668623	K1
3	0.9295517625	0.112002	6.270998	O1
4	1.9999969301	0.087477	0.294764	S2

```
5    1.8959911512  0.068525  6.088107  N2
 6    0.9972036083  0.060526  5.693939 P1
 7    0.0516620149  0.027059  3.169843
 8    1.4262524937  0.029294  3.779874
 9    1.1098648846  0.024852  1.545104
10    0.4148890439  0.040287  2.839791  vv=    1.4173545 m0= 0.06505


Latitude: -66.125519 Longitude: 280.405495
    freqency       amplitude   phase
 1    1.9322715019  0.243559  3.197524 M2
 2    1.0027237507  0.135149  4.713791 K1
 3    0.9295558576  0.120175  6.163970 O1
 4    1.9999972642  0.084556  0.370234 S2
 5    1.8959829095  0.065164  0.006977 N2
 6    1.9049536963  0.043620  3.963417
 7    0.2882127665  0.038028  0.897952
 8    0.8073343432  0.033031  0.512909
 9    0.1900934554  0.029407  4.666463
10    0.2004151246  0.026819  4.456079  vv=    1.6118140 m0= 0.06835


Latitude: -66.093498 Longitude: 281.806583
    freqency       amplitude   phase
 1    1.9322728988  0.249569  3.163803 M2
 2    1.0027114534  0.126662  5.132785 K1
 3    0.9295696807  0.115785  5.733053 O1
 4    1.9999958763  0.085736  0.436807 S2
 5    1.8959798612  0.060372  0.083465 N2
 6    0.9972966478  0.053004  3.049961 P1
 7    0.6057042263  0.044336  4.329572
 8    1.7158329744  0.037863  4.099537
 9    1.5993206667  0.032063  0.382270
10    0.7094872917  0.028131  1.062462  vv=    2.1722955 m0= 0.07935
```

REFERENCES

Alcock, G. A. and D. E. Cartwright, Some experiments with ‘orthotides’, *Geophys. J. Roy. Astron. Soc.*, 54, 681-696, 1978.

Andersen, O., Ocean tides in the northern North Atlantic and adjacent seas from ERS 1 altimetry, *J. Geophys. Res.*, 99(C11), 22557-22573, 1994.

Andersen, O., Global ocean tides from ERS 1 and TOPEX/POSEIDON altimetry, *J. Geophys. Res.*, 100(C12), 25249-25259, 1995.

Aoki, S., T. Ozawa, K. Shibuya and A. Masuyama, Ocean tide observed with differential GPS technique in Lützow-Holm Bay, Antarctica. *Journal of the Geodetic Society of Japan*, Vol. 47, No. 1, 181-186, 2001.

Calman, Y., Introduction to sea-surface topography from satellite altimetry, John Hopkins APL Technical Digest, Laurel Md, Vol. 8, No. 2, 206-211, 1987.

Cartwright, D. E. and R. J. Tayler, New computations of the tide-generating potential, *Geophys. J. Roy. Astron. Soc.*, 23, 45-74, 1971.

Cartwright, D. E. and A. C. Edden, Corrected tables of the tidal harmonics, *Geophys. J. Roy. Astron. Soc.*, 33, 253-264, 1973.

Cartwright, D. E. and R. D. Ray, Ocean tides from Geosat altimetry, *J. Geophys. Res.*, 95, C3, 3069-3090, 1990.

Cartwright, D. E., and R. D. Ray, Energetics of global ocean tides from Geosat altimetry, *J. Geophys. Res.*, 96, 16897-16912, 1991.

Casotto, S., Nominal ocean tide models for TOPEX/POSEIDON orbit determination, Ph.D dissertation, Center for Space Research, The University of Texas at Austin, 1989.

Darwin, G. H., Report of a committee for the harmonic analysis of tidal observations, *Brit. Ass. Rep.*, 48-118, 1883.

Desai, S. D. and J. M. Wahr, Empirical ocean tide models estimated from TOPEX/POSEIDON altimetry, *J. Geophys. Res.*, 100(C12), 25205-25228, 1995.

Desai, S. D., J. M. Wahr, and Y. Chao, Error analysis of empirical ocean tide models estimated from TOPEX/POSEIDON altimetry, *J. Geophys. Res*., 102(C11), 25157-25172, 1997.

Doodson, A. T., The harmonic development of the tide-generating potential, *Proc. Roy. Soc.*, A, 100, 305-329, 1921.

Dorandeu, J. and P. Y. Le Traon, Effects of global mean atmospheric pressure variations on mean sea level changes from TOPEX/POSEIDON, *Journal of Atmospheric and Oceanic Technology*, Vol.16, Issue 9, 1279-1283, 1999.

Eanes, R and S. Bettadpur, The CSR3.0 global ocean tide model, Center for Space Research, Technical Memorandum, CSR-TM-95-06, The Univ. of Texas at Austin, 1995.

Egbert, G. D., A. F. Bennett and M.G. Foreman, Topex/Poseidon tides estimated using a global inverse model, *J. Geophys. Res*., 99, 24821-24852, 1994.

Egbert G. D. and S. Y. Erofeeva, Efficient inverse modeling of the barotropic ocean tides, *Journal of Atmospheric and Oceanic Technolgy*, Vol.19, N2, 183-204, 2002.

Fricker, H. A. and L. Padman, Tides on Filchner-Ronne Ice Shelf from ERS radar altimetry, *Geophysical Res. Letters*, 29(12), 1622, 10.1029/2001GL014175, 2002.

Groves, G. W. and R. W. Reynolds, An orthogonalized convolution method of tide prediction, *J. Geophys. Res*., 80, 4131-4138, 1975.

IERS Conventions (2000), McCarthy D. (Ed), Observatoire de Paris, August 2000.

Jackson, D. D., The use of *a priori* data to resolve non-uniqueness in linear inversion, *Geophys. J. Roy. Astron. Soc*., 57, 137-157, 1979.

Kaula, W. M., The Terrestrial Environment: solid earth and ocean physics, NASA Rep. Study at Williamstown, MA, NASA CR-1579, 1969.

Kowalik, Z. and A. Yu. Proshutinsky, The Arctic Ocean tides, In: The Polar Oceans and their Role in Shaping the Global Environment AGU, 137-158, 1994.

Lambeck, K., Geophysical Geodesy: The slow deformation of the earth, Oxford University Press, 1988.

Lefèvre, F., F. H Lyard, and C. Le Provost, FES98: A new global tide finite element solution independent of altimetry. *Geophys. Res. Letters*, 27(17), 2717-2720, 2000.

Le Provost, C., An analysis of Seasat altimeter measurements over a coastal area: The English Channel. *J. Geophys. Res*. 105, 64, 8707-8725, 1983.

Le Provost, C. and P. Vincent, Extensive test of precision for a finite element model of ocean tides, *J. of Comput. Phys*., 65, 273-291, 1986.

Le Provost, C., M. L. Genco, F. Lyard, P. Vincent and P. Canceil, Tidal spectroscopy of the world ocean tides from a finite element hydrodynamic model, *J. Geophys. Res.*, 99(C12), 24777-24798, 1994.

Le Provost, C., Ocean tides, In: Satellite altimetry and earth sciences, Lee-lueng Fu and Anny Cazenave (Eds.), International Geophysics Series, Vol.69, Academic Press, 267-303, 2001.

Lorell, J., E. Colquitt and R. J. Anderle, Ionospheric correction for SEASAT altimeter height measurement. *J. Geophys. Res.*, 87(C5), 3207-3212, 1982.

Matsumoto, K., T. Takanezawa and M. Ooe, Ocean tide models developed by assimilating TOPEX/POSEIDON altimeter data into hydrodynamic model: A global model and a regional model around Japan, *J. of Oceanography*, 56, 567-581, 2000.

Mautz, R., Solving non-linear adjustment problems by heuristic optimization. In: *Proceedings of the Third Turkish-German Joint Geodetic Days*, Istanbul, Vol. 2, 791-797, 1999.

Mautz, R., Solving nonlinear adjustment problems by global optimization, *Boll. Geod. Sci. Aff.*, N. 2 , 123-134, 2002.

Metzig, R., R. Dietrich, W. Korth, J. Perlt, R. Hartmann, and W. Winzer, Horizontal ice velocity estimation and grounding zone detection in the surroundings of Schirmacheroase, Antarctica, using SAR interferometry, *Polarforschung*, 67(1/2), 7-14, 2000.

Munk, W. H. and D. E. Cartwright, Tidal spectroscopy and prediction, *Phil. Trans. Roy. Soc.* A, 259, 533-581, 1966.

Padman, L., R. Robertson and K. W. Nicholls, Modeling tides in the southern Weddell Sea: Updated model with new bathymetry from ROPEX, *Filchner-Ronne Ice Shelf Program*, Report No. 12, Alfred-Wegener Institute, Bremerhaven, Germany, 65-73, 1998.

Padman, L., D. MacAyeal and E. Rignot, Analysis of sub-ice-shelf tides in the Weddell Sea using SAR interferomerty, *Filchner-Ronne Ice Shelf Program*, Report No. 13, Alfred-Wegener Institute, Bremerhaven, Germany, 60-65,1999.

Padman, L., H. A. Fricker, R. Coleman, S. Howard, and S. Erofeeva, A new tide model for the Antarctic Ice Shelves and Seas, *Annals of Glaciology*, 34, 247-254, 2002.
Padman, L., S. Erofeeva and I. Joughin, Tides of the Ross Sea and Ross Ice Shelf cavity, *Antarctic Science*, 15(01), 31-40, 2003.

Padman, L. and S. Erofeeva, A barotropic inverse tidal model for the Arctic Ocean, *Geophys. Res. Letters*, 31(2)**,** L02303, 10.1029/2003GL019003, 2004.

Ponte, R. M., D. A. Salstein and R. D. Rosen, Sea level response to pressure forcing in a barotropic numerical model, *J. Phys. Oceanography*, 21, 1043-1057, 1991.

Ray, R. D., R. J. Eanes and B. F. Chao, Detection of tidal dissipation in the solid earth by satellite tracking and altimetry, *Nature*, 381, 595-597, 1996.

Rignot, E., Tidal motion, ice velocity and melt rate of Petermann Gletscher, Greenland, measured from radar interferometry. *J. Glaciology*, 42(142), 476-485, 1998.

Rignot, E., L. Padman, D. MacAyeal, and M. Schmeltz, Observation of ocean tides below the Filchner-Ronne ice shelf, Antarctica, using SAR interferometry: Comparison with tide model predictions, *J. Geophys. Res.*, 105(C8), 19615-19630, 2000.

Robertson, R., L. Padman, and G. Egbert, Tides in the Weddell Sea, In: Ocean, Ice, and Atmosphere: Interactions at the Antarctic Continental Margin, *Antarctic Research Series* 75, edited by S. Jacobs and R. Weiss, AGU, Washington DC, 341-369, 1998.

Saastamoinen, J., Atmospheric correction for the troposphere and stratosphere in radio ranging of satellites, Geophysical Monograph 15, American Geophysical Union, 1972.

Schrama, E. J. O. and R. D. Ray, A preliminary tidal analysis of TOPEX/POSEIDON altimetry, *J. Geophys. Res*., 99(C12), 24799-24808, 1994.

Schureman, P., Manual of harmonic analysis and prediction of tides, U.S. Coast and Geodetic Survey, Special Publication No. 98, 1971.

Schwiderski, E. W., Ocean Tides, Part I: Global ocean tidal equations, *Mar. Geod*., 3, 161-217, 1980.

Seeber, G., Satellite Geodesy: Foundations, Methods, and Applications, Walter de Gruyter, New York, 1993.

Shum, C. K., P. L. Woodworth, O. B. Andersen, G. D. Egbert, O. Francis, C. King, S. M. Klosko, C. Le Provost, X. Li, J-M Molines, M. E. Parke, R. D. Ray, M. G. Schlax, D. Stammer, C. C. Tiemey, P. Vincent and C. I. Wunsch, Accuracy assessment of recent ocean tide models, *J. Geophys. Res*. 102, C11, 25173-25194, 1997.

Shum, C. K., N. H. Yu and M. Charles, Recent advances in ocean tidal science, *Journal of the Geodetic Society of Japan*, Vol. 47, No. 1, 528-537, 2001.
Smith, A., Application of satellite altimetry for global ocean tide modeling, PhD dissertation, Delft University Press, 1999.

Taff, L. G. , Celestial Mechanics: A computational guide for the practitioner, John Wiley & Sons, 1985.

Tapley, B. D., J. B. Lundberg and G. H. Born, The SEASAT altimeter wet tropospheric range correction, *J. Geophys. Res*., Vol. 87, 3213-3220, 1982.

Wahr, J. M., Deformation induced by polar motion, *J. Geophys. Res*., Vol. 90, 9363-9368, 1985.

Williams, R. and E. Robinson, The ocean tide in the southern Ross Sea, *J. Geophys. Res*., 85(C11), 6689-6696, 1980.